

The ATLAS 5.5 GHz Survey of the Extended Chandra Deep Field South: The Second Data Release

M.T. Huynh,^{1*} M.E. Bell,² A.M. Hopkins,³ R.P. Norris,² N. Seymour⁴

¹ *International Center for Radio Astronomy Research, M468, University of Western Australia, Crawley, WA 6009, Australia*

² *CSIRO Astronomy and Space Science (CASS), PO Box 76, Epping, NSW 1710, Australia*

³ *Australian Astronomical Observatory, PO Box 915, North Ryde, NSW 1670, Australia*

⁴ *International Center for Radio Astronomy Research, Curtin University, Perth, WA, Australia*

7 September 2015

ABSTRACT

We present a new image of the 5.5 GHz radio emission from the extended Chandra Deep Field South. Deep radio observations at 5.5 GHz were obtained in 2010 and presented in the first data release. A further 76 hours of integration has since been obtained, nearly doubling the integration time. This paper presents a new analysis of all the data. The new image reaches 8.6 μ Jy rms, an improvement of about 40% in sensitivity. We present a new catalogue of 5.5 GHz sources, identifying 212 source components, roughly 50% more than were detected in the first data release. Source counts derived from this sample are consistent with those reported in the literature for $S_{5.5\text{GHz}} > 0.1$ mJy but significantly lower than published values in the lowest flux density bins ($S_{5.5\text{GHz}} < 0.1$ mJy), where we have more detected sources and improved statistical reliability. The 5.5 GHz radio sources were matched to 1.4 GHz sources in the literature and we find a mean spectral index of -0.35 ± 0.10 for $S_{5.5\text{GHz}} > 0.5$ mJy, consistent with the flattening of the spectral index observed in 5 GHz sub-mJy samples. The median spectral index of the whole sample is $\alpha_{\text{med}} = -0.58$, indicating that these observations may be starting to probe the star forming population. However, even at the faintest levels ($0.05 < S_{5.5\text{GHz}} < 0.1$ mJy), 39% of the 5.5 GHz sources have flat or inverted radio spectra. Four flux density measurements from our data, across the full 4.5 to 6.5 GHz bandwidth, are combined with those from literature and we find 10% of sources ($S_{5.5\text{GHz}} \gtrsim 0.1$ mJy) show significant curvature in their radio spectral energy distribution spanning 1.4 to 9 GHz.

Key words: galaxies: evolution — radio continuum: galaxies

1 INTRODUCTION

A fundamental question in astrophysics today is how galaxies and their main constituent parts, stars and black-holes, form and evolve over cosmic time. A link between black holes, or active galactic nuclei (AGN), and the stellar growth of galaxies is suggested by scaling relations such as that between the black hole mass and stellar bulge mass (e.g. Magorrian et al. 1998). An intimate connection between AGN and star formation in galaxies is further suggested by the similar decline in AGN activity (Hasinger et al. 2005; Aird et al. 2010) and star formation (Hopkins & Beacom 2006) from when the Universe was half its current age to today. Additionally, this connection between galaxy and AGN

evolution is reflected in the general shift of these processes from high mass galaxies in the distant Universe to low mass galaxies locally (Cowie et al. 1996; Hasinger et al. 2005; Juneau et al. 2005; Mobasher et al. 2009), commonly referred to as downsizing. Radio emission can be produced by both AGN and star-forming processes, hence radio wavelengths provide a unique dust-unbiased view of galaxy and AGN evolution.

The first large sky-area radio surveys were conducted more than 50 years ago and the current state-of-the art surveys (e.g. NVSS, Condon et al. 1998) now catalogue millions of sources. It is now well established that bright radio-loud sources (> 100 mJy) are associated with AGN activity (e.g. Condon 1984a). The normalised differential radio source counts, however, are observed to flatten below about 1 mJy in a way which cannot be explained by an extrapola-

* E-mail: minh.huynh@uwa.edu.au

tion of the population of radio-loud AGNs found at higher flux densities. Star formation in strongly evolving normal spiral galaxies (Condon 1984b, 1989) and starbursting galaxies (Windhorst et al. 1985; Rowan-Robinson et al. 1993) were suggested as new populations to explain this upturn. The upturn in the source counts was initially explained through modelling of source populations with no need to include a substantial AGN contribution (e.g. Hopkins et al. 1998). However, a growing number of studies are finding that lower luminosity AGN, both radio-loud and weakly radio emitting sources (radio-loud and radio-quiet AGN respectively), make a significant contribution to the sub-mJy population (Jarvis & Rawlings 2004; Huynh et al. 2008; Seymour et al. 2008; Smolčić et al. 2008; Padovani et al. 2009, 2011; Bonzini et al. 2013).

Star formation processes result in galaxies with a typical spectral index of $\alpha = -0.8$ at 1.4 GHz ($S \propto \nu^\alpha$, Condon 1992), consistent with optically-thin synchrotron emission from electrons accelerated by supernovae. The emission from the lobes of a radio jet are also synchrotron in nature, and hence also have steep spectral indices. A flat ($\alpha > -0.5$) or inverted ($\alpha > 0$) spectrum is usually attributed to the superposition of different self-absorbed components of varying sizes at the base of the radio jet of a radio-loud AGN. Thermal Bremsstrahlung (free-free) emission found in HII regions usually has a flatter spectral index but this becomes significant in normal galaxies only for rest-frame frequencies >10 GHz (e.g. Murphy 2009). The radio spectral index and radio spectral energy distribution can therefore provide important information on the nature of radio sources.

The spectral index of radio sources has been studied for a few decades. For the brightest sources (~ 1 Jy), the majority of 1.4 GHz-selected sources were found to be steep with a spectral index of $\alpha = -0.8$ (Condon 1984a), however a 5 GHz selected sample at similar flux densities shows a broad flat spectrum population of sources with $\alpha \sim 0$ (Witzel et al. 1979). This bright flat spectrum population is compact (unresolved) and more likely to be quasars than steep spectrum sources (Peacock & Wall 1981). The fraction of flat spectrum sources decreases with decreasing flux density such that the average spectral index is steep at the tens of mJy level (e.g. Condon & Ledden 1981; Owen et al. 1983). There is now emerging evidence that the spectral index flattens again at sub-mJy levels, but the nature and properties of these faint radio sources is still unclear. The flattening of the average spectral index at sub-mJy levels has been observed in faint 5 GHz selected samples (Prandoni et al. 2006; Huynh et al. 2012b) and recently confirmed in sub-mJy samples selected at even higher frequencies (>10 GHz, Whittam et al. 2013; Franzen et al. 2014). However sub-mJy sources selected at 1.4 GHz or 610 MHz do not appear to exhibit a flattening in their average spectral index (Ibar et al. 2009). The observed flattening of the spectral index in higher frequency samples is not easily reproduced from extrapolations of the 1.4 GHz population, indicating that either there is a new population of faint, flat spectrum sources which are missing from 1.4 GHz selected samples, or the higher frequency radio emission of the known 1.4 GHz population is not well-modelled.

In order to study the faint 5.5 GHz population we observed the extended Chandra Deep Field South with the Compact Array Broadband Backend (CABB; Wilson et al. 2011) on the Australia Telescope Compact Array. Our ob-

serving run in 2010 consisted of 144 hours of observations, and this was supplemented by initial pilot observations of 20 hours from August 2009. A total of 42 pointings was used to uniformly sample the full 30×30 arcmin eCDFS region at 6cm, achieving $\sim 12 \mu\text{Jy}$ rms over roughly 0.25 deg^2 with a restoring beam of 4.9×2.0 arcsec. The survey description, image reduction and catalogue were presented in Huynh et al. (2012b) (hereafter H12). Further 6cm observations of the extended Chandra Deep Field South were obtained in 2012 in a program to detect faint variable radio sources, nearly doubling the effective integration time. This paper presents a new and more sensitive 6cm image from a reduction of all the data. This new image covers 0.34 deg^2 with a typical sensitivity in the inner region of $\sim 9 \mu\text{Jy}$ rms, making it the largest mosaic ever made at 6cm to these depths. We describe the survey and wide-field wide-band imaging techniques in Section 2. In Section 3 we discuss the extraction and characterisation of sources and present the source catalogue. Source counts from the new data and an analysis of the radio spectral energy distribution of the sources are presented in Sections 4 and 5, respectively.

2 THE OBSERVATIONS

2.1 Observing Strategy

The extended Chandra Deep Field South (eCDFS) was observed with the Compact Array Broadband Backend (CABB; Wilson et al. 2011) on the Australia Telescope Compact Array (ATCA) with the full 2048 MHz bandwidth centred at 5.5 GHz. We chose a 42 pointing hexagonal mosaic with spacings of 5 arcmin (approximately 0.5 FWHM of the primary beam) to uniformly sample the full 30×30 arcmin eCDFS region, centered approximately at RA = 3h32m22s and Dec = $-27^\circ 48' 37''$ (J2000). The 20 hours in 2009 and 144 hours in 2010 were allocated under ATCA observing program C2028. This data resulted in a rms sensitivity of $11.9 \mu\text{Jy}$ and synthesised beam size of 4.9×2.0 arcsec (H12), under hereafter Epoch 1 and Data Release 1.

Further observations were obtained in 2012 via ATCA program C2670. The C2670 program was conceived as a blind search for sub-mJy level sources that are variable on time scales of months to roughly a year, with a secondary goal of testing the Variables and Slow Transients (VAST, Murphy et al. 2013) data pipeline. A total of 54 hours in May–June 2012 (Epoch 2) and 47 hours in August 2012 (Epoch 3) was allocated to C2670, and the data was taken using the mosaicing strategy of H12. The three epochs are summarised in Table 1. An analysis of the variable sources is presented in Bell et al. (2015). Here we present a reduction of the full dataset, i.e. all three epochs, to obtain the most sensitive image possible.

2.2 Wide-field Wide-band Imaging

The new generation of wide-band receivers on radio interferometers such as ATCA and the Very Large Array (VLA) have led to new challenges in radio imaging. The 2 GHz bandwidth is a significant fraction of the central frequency of the observations. The primary beam response, the synthesized beam and the flux density of most sources vary

Table 1. Summary of the ATCA observations used in this data release.

Program ID	Epoch and Date	Array	Net Integration Time (h)
C2028	1, 2009 Aug 12, 14	6D	13.8
C2028	1, 2010 Jan 5 – 15	6A	91.0
C2670	2, 2012 May 31 – June 4	6A	41.7
C2670	3, 2012 Aug 14 – 18	6D	34.3

significantly with frequency. One way to mitigate the issues with a large bandwidth is to divide uv data into sub-bands and then force nearly identical beam-sizes with an appropriate “robustness” parameter (Briggs 1995). This sub-division approach was used to image VLA data spanning 2 – 4 GHz (Condon et al. 2012). While the fractional bandwidth is less for our ATCA data centred at 5.5 GHz, we tested two imaging schemes: one where the uv data is not divided into sub-bands (hereafter full-band reduction), and a second scheme where the 2048 MHz CABB band is divided into 512 MHz sub-bands (hereafter sub-band reduction).

We used the Multichannel Image Reconstruction, Image Analysis and Display (MIRIAD) software package to reduce the CABB data. This is the standard package used for ATCA data and has undergone several enhancements since H12 to better handle the wide-band of CABB. These include an option to allow calibration task *gpcal* to solve for gain variation across the band and an option for *linmos* to apply several frequency-averaged primary beams instead of one primary beam across the full 2 GHz band. The full-band and sub-band reductions use the same calibration scheme. In the calibration step we set the number of frequency bins in *gpcal* to four (i.e. 512 MHz bins) and for the primary beam correction we set *linmos* to apply ten frequency bins. The 42 pointings were individually reduced and imaged. Automated flagging was performed using the MIRIAD task *pgflag*. *pgflag* is based on AOFLAGGER (Offringa et al. 2010) which was developed for LOFAR but now used at many telescopes.

The steps for the full-band reduction are similar to that in H12, but with some improvements to the cleaning and self calibration steps. We performed multi-frequency synthesis imaging with *invert* using the same robust weighting as H12, $\text{robust} = 1$, and set the image size to 2500×2500 pixels with 0.5 arcsec pixels. This is larger than H12 because the frequency varying primary beam response means a larger image is needed to capture the larger field of view at the low frequency end. Multi-frequency cleaning was performed with the task *mfclean* with the clean region set to about 9.6 arcmin. This extends to just beyond the 10% response level at 4.5 GHz, the lower end of the band, therefore encompassing the full region of interest. We found two iterations of phase self-calibration produced good results. The first iteration was performed with a model set from 100 *mfclean* iterations (i.e. bright sources only), and the second with the model set by cleaning to 4σ . The individual pointings were restored with the same beam, the average beam of the 42 pointings, 5.0×2.0 arcsec. The individual pointings were then mosaiced together using the task *linmos*, which applies the ten frequency-varying primary beams. The edges of each pointing beyond 9.5 arcmin were removed before the

combination, to discard the uncleaned areas with a very low primary beam response from the final mosaic.

In the sub-band reduction the calibrated data was split into 4 sub-bands of 512 MHz, resulting in fractional bandwidths of 0.09 – 0.11, much less than 1. Each sub-band was imaged with a different robust weighting that resulted in similar beam-sizes. Multi-frequency cleaning and self-calibration was then performed for each pointing and each sub-band using the same strategy as for the full-band reduction. The individual images were restored with the same beam, the average beam of the 4×42 images. Finally, as for the full-band reduction, the 4×42 images were mosaiced together using *linmos*.

2.3 Image Analysis: Sensitivity and Clean Bias

We used the MIRIAD task *sigest*, iteratively clipping the pixels, to estimate the noise in the inner 20×20 arcmin region of the full-band and sub-band mosaic. We find the noise in the full-band reduced mosaic is $8.6 \mu\text{Jy}/\text{beam}$, and $8.7 \mu\text{Jy}/\text{beam}$ for the sub-band reduced mosaic. The full-band reduced mosaic therefore has slightly lower noise than the sub-band reduced mosaic, at the 1% level. On visual inspection of the two mosaics the sidelobes around bright sources appear to be marginally more prominent in the sub-band reduction compared to the full-band reduction. This may be due to the better self-calibration from *mfclean* models produced in the full-band reduction, which goes deeper than the sub-band imaging and has better uv -coverage. We use the full-band reduced mosaic in the production of the catalogue.

The full-band mosaic is shown in Figure 1, where regions greater than 5 arcmin (~ 0.5 FWHM of the primary beam) of the outer pointings have been removed to minimise primary beam affects and avoid high levels of non-Gaussian noise which may affect the source extraction. The noise properties of this full-band mosaic were investigated using SExtractor (Bertin & Arnouts 1996). Briefly, SExtractor calculates the background and rms for a region (or ‘mesh’) around each pixel using a combination of clipping and mode estimation. SExtractor with mesh-sizes of 8 – 12 times the synthesized beam is known to produce good noise estimates of radio images (Schinnerer et al. 2007, 2010; Huynh et al. 2005, 2012a). Figure 2 shows the histogram of the pixels in the noise image generated by SExtractor, using a mesh-size of 10 times the synthesized beam. The peak in the distribution is $8.4 \mu\text{Jy}/\text{beam}$, broadly consistent with the *sigest* result of $8.6 \mu\text{Jy}/\text{beam}$ for the inner part of the mosaic. The median of the noise distribution is $9.3 \mu\text{Jy}/\text{beam}$, so half of the mosaic has an rms noise level lower than this. The tail at high noise levels ($>11 \mu\text{Jy}/\text{beam}$) is due to the higher levels of noise at the edge of the mosaic from the primary beam response and increased noise around bright sources.

When uv coverage is incomplete the cleaning process can redistribute flux from real sources on to noise peaks. This clean bias is generally only a problem for snapshot observations where uv coverage is poor. Although our uv coverage is good from the 180 hours split between 6A and 6D configurations, we performed tests to check the extent of the clean bias in the full-band mosaic. Point sources were injected into the uv data at random positions to avoid being confused with real sources. The uv data was then imaged

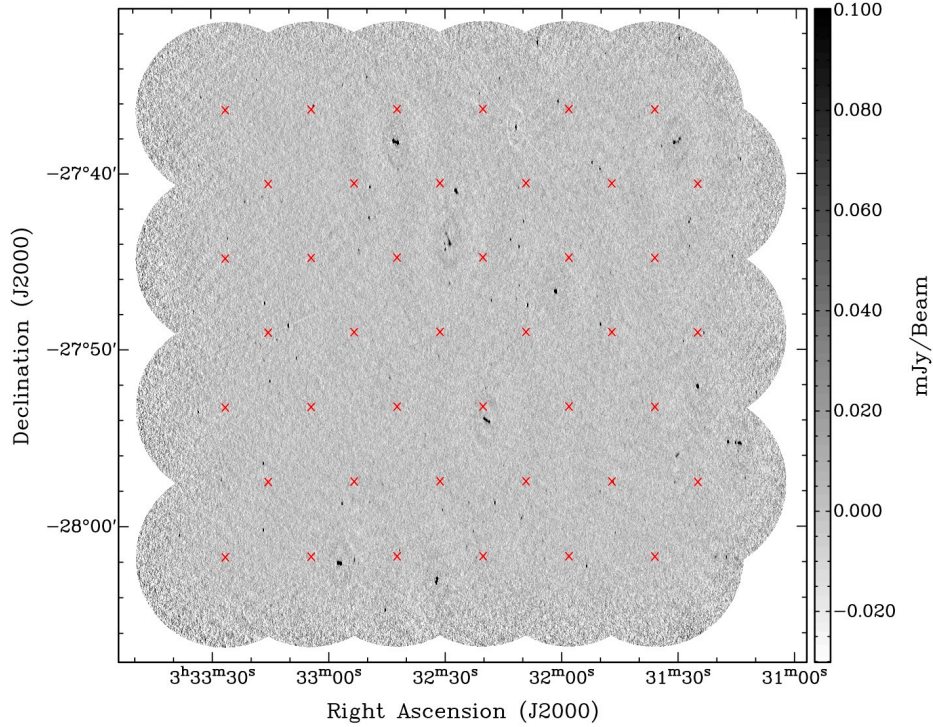


Figure 1. The eCDFs 5.5 GHz full-band mosaic with the greyscale set to the range -0.03 to 0.1 mJy. The red crosses mark the 42 individual pointings of the mosaic. The total area covered by this mosaic is 0.34 deg^2 .

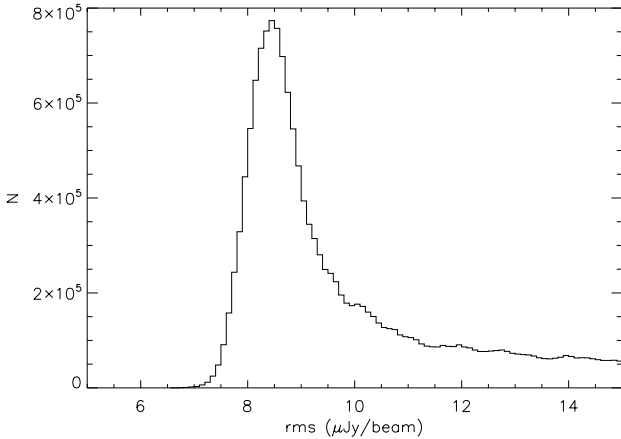


Figure 2. The noise distribution, as determined from the noise image generated by SExtractor.

with the same cleaning depth as the production images, and the source output flux densities compared to the input values. The fake sources were injected one at a time to avoid source confusion, and the process repeated 4000 times to obtain a large sampling. We find the median clean bias is $\sim 5\%$ for the faintest sources at $50 \mu\text{Jy}$ and it is negligible for brighter sources ($> 150 \mu\text{Jy}$). We therefore conclude clean bias is not a significant issue.

3 SOURCE EXTRACTION

There are many radio source extraction tools available, including AIPS and MIRIAD Gaussian fitting routines *sad*, *vsad* and *imsad*, the false discovery rate algorithm *sfind* (Hopkins et al. 2002), and newer codes such as Duchamp (Whiting 2012), BLOBCAT (Hales et al. 2012), and AEGERAN (Hancock et al. 2012). Most of these source finding algorithms use a simple S/N thresholding technique whereby a source is deemed a true source if it has a peak flux density, or pixel value, above a set threshold. Following our previous work in H12, we use the MIRIAD task *sfind* to search for sources. The *sfind* task implements a false-discovery rate algorithm (Miller et al. 2001), which compares the distribution of image pixels to that of an image containing only noise to return a list of source detections. The user set threshold is the fraction of sources which are allowed to be false, not a S/N.

We searched the full-band mosaic shown in Figure 1, which has a total area of 0.34 deg^2 . As in H12 we ran *sfind* with ‘rmsbox’ set to 10 synthesized beamwidths and ‘alpha’ set to 1. If the noise is perfectly Gaussian then setting ‘alpha’ to 1 returns a list of sources which is 99% reliable. Each *sfind* source was then individually fit as a point source and a Gaussian with MIRIAD task *imfit*. We identified 12 multiple component sources via visual inspection (see Figure 3). These sources exhibit classical core-lobe or lobe-lobe radio AGN morphology and are components of a single source. They were fitted as multiple Gaussians with *imfit* where necessary and the components listed individually in the final catalogue. There are 212 source components and 189 sources in the final catalogue.

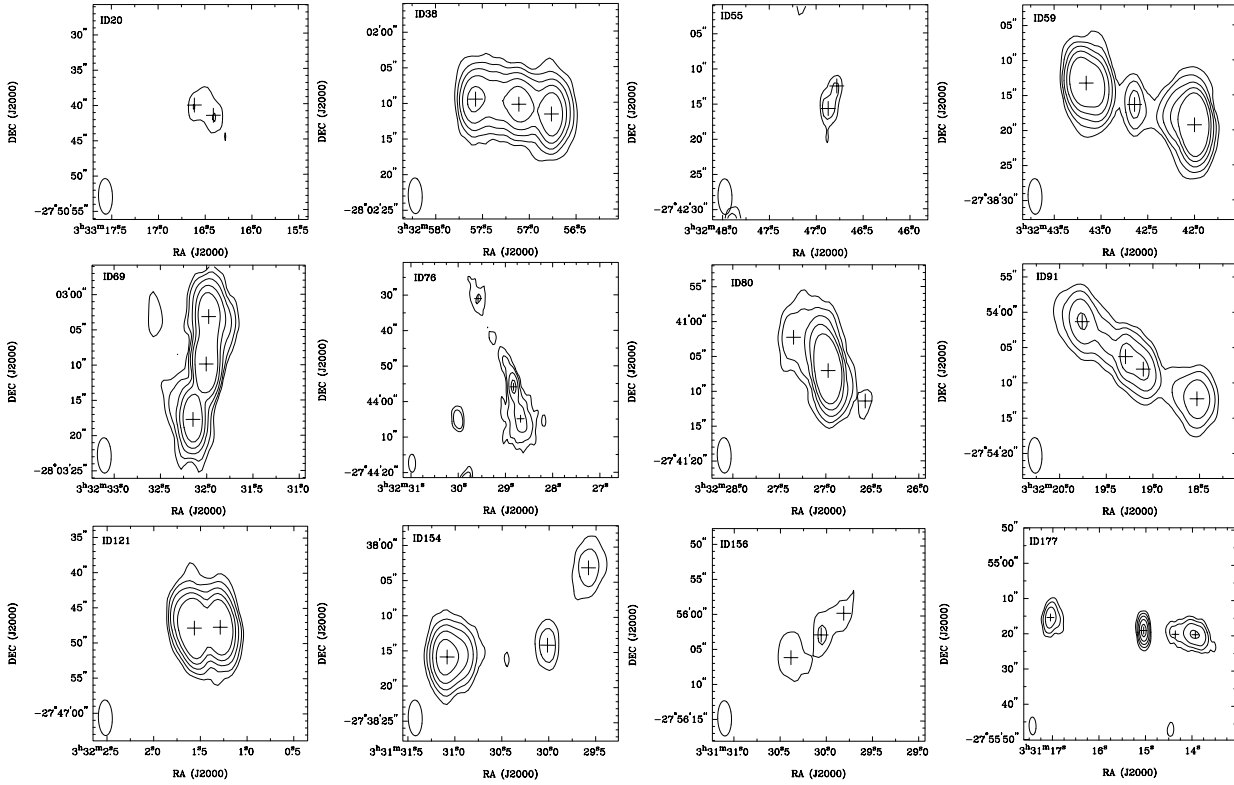


Figure 3. Contour images of the multiple sources in the catalogue. The images are 30×30 arcsec in size, except for IDs 76 and 177, which are 1×1 arcmin. The contour levels are set at 5, 10, 20, 40 and 80 times the local noise level. However IDs 20, 55 and 76 also have a 3 sigma contour to highlight more detail in the source morphology. The synthesized beam is shown in the bottom left corner. Crosses mark the positions of the catalogued components.

3.1 Deconvolution

The ratio of integrated to peak flux density gives a direct measure of the extension of a source. We performed the same analysis as in H12 to determine if a source is resolved, using the ratio of integrated flux to the peak flux (see Equation 1 of H12), where the peak flux is the peak of the fitted Gaussian. Whether a source is successfully deconvolved depends on the S/N ratio of the source and not just the synthesised beam-size. Using the Gaussian fits from *imfit*, we show the integrated flux density to peak flux density as a function of S/N in Figure 4.

Assuming the sources with $S_{\text{tot}}/S_{\text{peak}} < 1$ are due to noise then an envelope can be defined as:

$$S_{\text{tot}}/S_{\text{peak}} = 1 + a/(S_{\text{peak}}/\sigma)^b. \quad (1)$$

In H12 we defined this envelope with $a = 10$ and $b = 1.5$. Figure 4 shows the lower curve, Equation 1 mirrored across $S_{\text{tot}}/S_{\text{peak}} = 1$, sufficiently encompasses all the $S_{\text{tot}}/S_{\text{peak}} < 1$. Sources which lie above the envelope, Equation 1, are considered successfully deconvolved. We add the extra criterion that $S_{\text{tot}}/S_{\text{peak}} > 1.02$ to account for the uncertainty in Gaussian fitting, which would otherwise push compact bright sources over the deconvolved line. We find that 66/212 (31%) source components lie above the upper envelope and have $S_{\text{tot}}/S_{\text{peak}} > 1.02$, and we consider these to be successfully deconvolved (i.e. resolved).

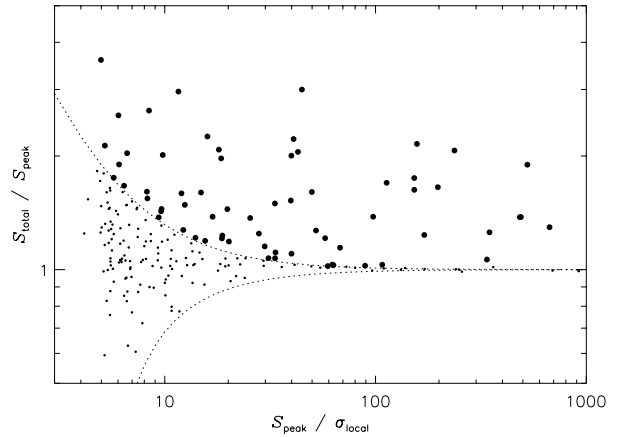


Figure 4. The ratio of integrated (S_{tot}) flux density to peak flux density (S_{peak}) as a function of source signal to noise (S_{peak}/σ). The dotted line shows the upper and lower envelopes of the flux ratio distribution that contains 90% of the unresolved sources. The large dots indicate sources which are deconvolved successfully and considered resolved.

3.2 The Source Catalogue

The source catalogue is reported in Table 2. Point-source measurements are given for sources which are not successfully deconvolved. The integrated source flux density and deconvolved source sizes from the Gaussian fits are given for the resolved, or successfully deconvolved, sources. Absorption

lute calibration errors dominate for high S/N sources, but internal fitting errors shown in Table 2 dominate for the majority of sources, which are low S/N.

Column (1) - ID. A letter, such as ‘a’, ‘b’, etc., indicates a component of a multiple source.

Column (2) - Source IAU name

Columns (3) and (4) - Source position: Right Ascension and Declination (J2000)

Column (5) - Point source flux density (μJy). (Peak flux density for deconvolved sources.)

Column (6) - Uncertainty in point source flux density (μJy). (Uncertainty in peak flux density for deconvolved sources.)

Column (7) - Integrated flux density (μJy). Zero indicates source is not successfully deconvolved and hence no integrated flux density is given.

Column (8) - Uncertainty in integrated flux density (μJy). Zero indicates source is not successfully deconvolved.

Column (9) - Deconvolved major axis (arcsec). Zero indicates source is not successfully deconvolved.

Column (10) - Deconvolved minor axis (arcsec). Zero indicates source is not successfully deconvolved.

Column (11) - Deconvolved position angle (degrees), measured from north through east. Zero indicates source is not successfully deconvolved.

Column(12) - Local noise level, rms, in μJy .

3.3 Flux comparison with Data Release 1 and VLA survey

Transients and sources that are variable on timescales of months and years are discussed in a separate paper (Bell et al. 2015), but as a consistency check we compared the flux densities of the sources in this release with Data Release 1 (H12) flux densities. The flux densities for sources detected in both data releases are shown in Figure 5. We find no significant difference in the average flux densities of sources between the data releases. The ratio of DR2 (this work) to DR1 (H12) flux densities has a mean of 1.02 ± 0.01 and median of 1.01.

We also compare our flux densities with that from the VLA. Four VLA pointings were used to cover a region of approximately 20×20 arcmin in the eCDFs at 4.9 GHz. The sensitivity of the VLA observations ranged from $7 \mu\text{Jy}/\text{beam}$ rms at the pointing centers to $50 \mu\text{Jy}/\text{beam}$ rms at the edges (Kellermann et al. 2008). The resolution of the VLA 4.9 GHz image is about 3.5 arcsec, which is similar to the synthesized beam of our ATCA imaging, but to minimise resolution effects we compared the single component sources only. We compared the VLA 4.9 GHz flux densities with our 4.8 GHz sub-band flux densities to minimise spectral index effects (Figure 5). We find ATCA/VLA flux density ratio has a mean of 1.13 ± 0.09 and median of 1.09. For a spectral index of $\alpha = -0.8$ ($S \propto \nu^\alpha$) we expect the ATCA flux densities to be about a few percent greater than the VLA measurements, if the VLA and ATCA are calibrated on the same scale. The ATCA flux densities therefore appear to be $\sim 10\%$ greater than VLA flux densities for this frequency, which is generally consistent with our earlier estimate of ATCA flux densities being $\sim 20\%$ greater (H12). Our earlier estimate included faint ($< 3\sigma$) VLA 6cm sources which are excluded in this analysis. The ATCA and VLA flux density scales both claim

to be tied to within a few percent of the Baars et al. (1977) scale, so the source of this discrepancy is unclear.

3.4 Completeness and Flux Boosting

As in H12, we performed Monte-Carlo simulations to estimate the completeness of the source catalogue. Artificial point sources were injected on to random locations of the mosaic and then extracted using the same method that produced the catalogue. Although the hexagonal mosaicing pattern results in fairly uniform noise across most of the image, the edges of the mosaic have increased noise levels due to the primary beam response and therefore lower completeness. We recovered the overall completeness level of the generated catalogue by injecting sources over the full area of the mosaic from which sources are extracted for the catalogue. We injected 8000 artificial sources for reliable statistics, and injected a single source at a time, to avoid confusion effects. The input flux density varied from 20 to 2000 μJy to sample the full range of interest. The completeness as a function of flux density is shown in Figure 6. The completeness rises steeply from about 20% at 40 μJy to approximately 90% at 100 μJy . The 50% completeness level occurs at approximately 52 μJy (cf. the 50% completeness level of 75 μJy for Data Release 1; H12).

Sources that lie on a noise peak have increased flux densities and therefore have a higher probability of being detected, while sources which lie on a noise trough have decreased flux densities and may be excluded altogether. This can lead to a flux boosting of sources, and this effect is strongest in the faintest flux density bins. The degree of flux boosting can be estimated from the ratio of output to input flux density of the simulations (Figure 6). In the faintest bins we find that flux densities are boosted by about 14% at 50 μJy and 28% at 40 μJy , on average. The flux boosting is negligible for sources with flux densities brighter than about 75 μJy .

Estimates of the positional accuracy of the catalogue can be made by comparing input and output positions. The median of the RA and Dec offsets as a function of input flux density is shown in Figure 7. The positional accuracy can be estimated from the standard deviation in the offsets. We find that at the faintest levels (40 μJy) the RA and Dec uncertainties are approximately 0.2 and 0.4 arcsec, respectively. The total positional accuracy is ~ 0.25 arcsec or better for sources that are brighter than 0.1 mJy.

3.5 Source Size and Resolution Bias

Weak and extended radio sources may have peak flux densities that fall below the detection threshold, leading to so-called resolution bias. To derive source counts which are complete in terms of total flux density the resolution bias must be determined. As in H12 we follow the formalism of Prandoni et al. (2001) and Huynh et al. (2005) in calculating the resolution bias.

In brief, the maximum size (θ_{max}) a source of total flux density S_{tot} can have is $S_{\text{tot}}/\sigma_{\text{det}} = \theta_{\text{max}}^2/b_{\text{min}}b_{\text{max}}$, where b_{min} and b_{max} are the synthesized beam FWHM axes and σ_{det} is the detection limit. Since the *sfind* detection limit varies across the image, we take the 50% completeness level

Table 2. The ATLAS 5.5 GHz Data Release 2 Catalogue

ID	IAU name	RA (J2000)	Dec (J2000)	S_{pnt} (μ Jy)	dS_{pnt} (μ Jy)	S_{int} (μ Jy)	dS_{int} (μ Jy)	Decon Bmajor	Decon Bminor	Decon PA	σ_{local}
1	ATCDF5 J0033348.75-280233.1	03:33:48.75	-28:02:33.1	283	30	0	0	0.00	0.00	0.0	30.5
2	ATCDF5 J0033341.31-273809.0	03:33:41.31	-27:38:09.0	306	17	0	0	0.00	0.00	0.0	22.4
3	ATCDF5 J0033338.35-280030.9	03:33:38.35	-28:00:30.9	544	27	0	0	0.00	0.00	0.0	16.9
4	ATCDF5 J0033334.58-274751.3	03:33:34.58	-27:47:51.3	155	14	0	0	0.00	0.00	0.0	15.4
5	ATCDF5 J0033333.43-275332.9	03:33:33.43	-27:53:32.9	505	12	0	0	0.00	0.00	0.0	14.0
6	ATCDF5 J0033333.14-273932.7	03:33:33.14	-27:39:32.7	96	12	0	0	0.00	0.00	0.0	14.4
7	ATCDF5 J0033333.14-274602.1	03:33:33.14	-27:46:02.1	95	14	0	0	0.00	0.00	0.0	14.2
8	ATCDF5 J0033332.56-273538.9	03:33:32.56	-27:35:38.9	421	13	0	0	0.00	0.00	0.0	14.1
9	ATCDF5 J0033327.84-275726.1	03:33:27.84	-27:57:26.1	113	12	155	38	2.59	1.31	16.3	12.0
10	ATCDF5 J0033325.85-274343.0	03:33:25.85	-27:43:43.0	231	12	0	0	0.00	0.00	0.0	10.2
11	ATCDF5 J0033322.74-275459.9	03:33:22.74	-27:54:59.9	93	12	0	0	0.00	0.00	0.0	10.5
12	ATCDF5 J0033321.31-274138.6	03:33:21.31	-27:41:38.6	265	10	0	0	0.00	0.00	0.0	10.7
13	ATCDF5 J0033320.60-274910.0	03:33:20.60	-27:49:10.0	56	9	0	0	0.00	0.00	0.0	10.1
14	ATCDF5 J0033319.05-273530.6	03:33:19.05	-27:35:30.6	72	18	0	0	0.00	0.00	0.0	10.2
15	ATCDF5 J0033318.71-274940.2	03:33:18.71	-27:49:40.2	76	10	0	0	0.00	0.00	0.0	10.1
16	ATCDF5 J0033318.29-273440.0	03:33:18.29	-27:34:40.0	108	15	0	0	0.00	0.00	0.0	10.4
17	ATCDF5 J0033316.94-274121.9	03:33:16.94	-27:41:21.9	74	11	120	40	2.70	1.74	-34.1	9.0
18	ATCDF5 J0033316.76-280016.1	03:33:16.76	-28:00:16.1	1286	15	0	0	0.00	0.00	0.0	9.3
19	ATCDF5 J0033316.73-275630.4	03:33:16.73	-27:56:30.4	697	9	0	0	0.00	0.00	0.0	9.5
20A	ATCDF5 J0033316.61-275040.0	03:33:16.61	-27:50:40.0	55	14	0	0	0.00	0.00	0.0	9.6
20B	ATCDF5 J0033316.41-275041.5	03:33:16.41	-27:50:41.5	55	15	0	0	0.00	0.00	0.0	9.6
21	ATCDF5 J0033316.35-274725.1	03:33:16.35	-27:47:25.1	1298	15	0	0	0.00	0.00	0.0	9.8
22	ATCDF5 J0033314.98-275151.4	03:33:14.98	-27:51:51.4	704	13	0	0	0.00	0.00	0.0	8.8
23	ATCDF5 J0033314.84-280432.1	03:33:14.84	-28:04:32.1	246	14	0	0	0.00	0.00	0.0	13.9
24	ATCDF5 J0033313.13-274930.5	03:33:13.13	-27:49:30.5	137	11	0	0	0.00	0.00	0.0	8.9
25	ATCDF5 J0033312.63-275231.8	03:33:12.63	-27:52:31.8	67	12	0	0	0.00	0.00	0.0	8.3
26	ATCDF5 J0033311.80-274138.7	03:33:11.80	-27:41:38.7	100	7	0	0	0.00	0.00	0.0	8.6
27	ATCDF5 J0033310.19-274842.2	03:33:10.19	-27:48:42.2	10114	54	0	0	0.00	0.00	0.0	11.0
28	ATCDF5 J0033309.73-274802.0	03:33:09.73	-27:48:02.0	89	12	127	44	3.73	0.72	19.6	9.2
29	ATCDF5 J0033308.17-275033.3	03:33:08.17	-27:50:33.3	499	8	0	0	0.00	0.00	0.0	9.1
30	ATCDF5 J0033305.11-274028.6	03:33:05.11	-27:40:28.6	51	12	0	0	0.00	0.00	0.0	8.5
31	ATCDF5 J0033304.45-273802.1	03:33:04.45	-27:38:02.1	63	10	0	0	0.00	0.00	0.0	8.5
32	ATCDF5 J0033303.73-273611.1	03:33:03.73	-27:36:11.1	300	14	333	28	1.96	0.51	-3.9	9.0
33	ATCDF5 J0033302.68-275642.7	03:33:02.68	-27:56:42.7	61	10	0	0	0.00	0.00	0.0	8.0
34	ATCDF5 J0033301.82-273637.2	03:33:01.82	-27:36:37.2	65	8	0	0	0.00	0.00	0.0	9.2
35	ATCDF5 J0033301.83-274540.4	03:33:01.83	-27:45:40.4	49	8	0	0	0.00	0.00	0.0	8.8
36	ATCDF5 J0033259.30-273534.5	03:32:59.30	-27:35:34.5	60	10	0	0	0.00	0.00	0.0	9.7
37	ATCDF5 J0033259.21-274325.4	03:32:59.21	-27:43:25.4	63	14	0	0	0.00	0.00	0.0	9.4
38A	ATCDF5 J0033257.11-280209.4	03:32:57.11	-28:02:09.4	1428	48	2426	166	2.74	1.94	-39.0	12.7
38B	ATCDF5 J0033257.11-280210.2	03:32:57.11	-28:02:10.2	1961	49	4222	226	3.71	1.17	78.7	12.5
38C	ATCDF5 J0033256.76-280211.6	03:32:56.76	-28:02:11.6	2413	60	3990	184	2.32	2.12	56.5	12.2
39	ATCDF5 J0033256.47-275848.3	03:32:56.47	-27:58:48.3	921	14	949	26	1.18	0.16	3.9	8.6
40	ATCDF5 J0033256.26-273500.7	03:32:56.26	-27:35:00.7	122	10	0	0	0.00	0.00	0.0	10.3
41	ATCDF5 J0033253.34-280159.3	03:32:53.34	-28:01:59.3	564	18	683	40	3.31	0.31	-0.9	9.8
42	ATCDF5 J0033252.89-273838.5	03:32:52.89	-27:38:38.5	52	7	0	0	0.00	0.00	0.0	8.3
43	ATCDF5 J0033252.24-280209.7	03:32:52.24	-28:02:09.7	65	10	0	0	0.00	0.00	0.0	10.5
44	ATCDF5 J0033252.06-274425.6	03:32:52.06	-27:44:25.6	203	14	0	0	0.00	0.00	0.0	8.8
45	ATCDF5 J0033251.83-274436.7	03:32:51.82	-27:44:36.7	70	13	0	0	0.00	0.00	0.0	9.0
46	ATCDF5 J0033251.83-275717.4	03:32:51.83	-27:57:17.4	51	9	0	0	0.00	0.00	0.0	8.4
47	ATCDF5 J0033249.95-273432.9	03:32:49.95	-27:34:32.9	139	16	206	59	3.63	0.94	-19.6	11.1
48	ATCDF5 J0033249.93-273446.2	03:32:49.93	-27:34:46.2	59	11	0	0	0.00	0.00	0.0	10.7
49	ATCDF5 J0033249.43-274235.4	03:32:49.43	-27:42:35.4	846	20	867	36	0.92	0.24	4.8	9.5
50	ATCDF5 J0033249.20-274050.8	03:32:49.20	-27:40:50.8	2366	28	0	0	0.00	0.00	0.0	9.5
51	ATCDF5 J0033249.32-275844.1	03:32:49.32	-27:58:44.1	70	9	109	27	3.41	1.45	16.8	8.5
52	ATCDF5 J0033248.54-274934.0	03:32:48.54	-27:49:34.0	44	10	0	0	0.00	0.00	0.0	8.4
53	ATCDF5 J0033247.89-274232.7	03:32:47.89	-27:42:32.7	76	12	0	0	0.00	0.00	0.0	10.1
54	ATCDF5 J0033246.95-273903.3	03:32:46.95	-27:39:03.3	50	10	0	0	0.00	0.00	0.0	9.1
55A	ATCDF5 J0033246.87-274215.6	03:32:46.87	-27:42:15.6	72	14	0	0	0.00	0.00	0.0	9.1
55B	ATCDF5 J0033246.78-274212.4	03:32:46.78	-27:42:12.4	59	17	0	0	0.00	0.00	0.0	8.9
56	ATCDF5 J0033245.37-280449.9	03:32:45.37	-28:04:49.9	612	31	933	106	3.11	0.38	-39.6	15.4
57	ATCDF5 J0033244.26-275141.0	03:32:44.26	-27:51:41.0	126	16	0	0	0.00	0.00	0.0	8.1
58	ATCDF5 J0033244.05-275144.0	03:32:44.05	-27:51:44.0	88	15	0	0	0.00	0.00	0.0	8.1
59A	ATCDF5 J0033243.15-273813.2	03:32:43.15	-27:38:13.2	4612	257	9538	792	3.58	1.62	64.5	19.5
59B	ATCDF5 J0033242.64-273816.3	03:32:42.64	-27:38:16.3	519	29	647	71	2.44	1.00	4.8	18.6
59C	ATCDF5 J0033241.99-273819.2	03:32:41.99	-27:38:19.2	10668	441	13820	826	1.82	1.32	23.1	15.9
60	ATCDF5 J0033242.62-273825.7	03:32:42.62	-27:38:25.7	74	13	0	0	0.00	0.00	0.0	12.5
61	ATCDF5 J0033241.99-273949.4	03:32:41.99	-27:39:49.4	129	9	0	0	0.00	0.00	0.0	9.0
62	ATCDF5 J0033241.62-280127.9	03:32:41.62	-28:01:27.9	124	9	0	0	0.00	0.00	0.0	8.7
63	ATCDF5 J0033240.82-275547.4	03:32:40.82	-27:55:47.4	53	5	0	0	0.00	0.00	0.0	7.8
64	ATCDF5 J0033239.47-275301.5	03:32:39.47	-27:53:01.5	52	9	0	0	0.00	0.00	0.0	8.5
65	ATCDF5 J0033237.73-275000.9	03:32:37.73	-27:50:00.9	56	13	0	0	0.00	0.00	0.0	8.6
66	ATCDF5 J0033237.23-275748.2	03:32:37.23	-27:57:48.2	56	7	0	0	0.00	0.00	0.0	9.0
67	ATCDF5 J0033234.93-275455.9	03:32:34.93	-27:54:55.9	54	10	0	0	0.00	0.00	0.0	8.6
68	ATCDF5 J0033232.55-280303.0	03:32:32.55	-28:03:03.0	105	12	0	0	0.00	0.00	0.0	12.9
69A	ATCDF5 J0033232.14-280317.7	03:32:32.14	-28:03:17.7	2254	77	2785	196	1.98	1.12	0.2	13.2
69B	ATCDF5 J0033232.00-280309.8	03:32:32.00	-28:03:09.8	4525	177	4813	401	1.8	0.08	-17.3	13.4
69C	ATCDF5 J0033231.97-280303.1	03:32:31.97	-28:03:03.1	2042	109	3323	389	3.28	1.83	1.5	13.4
70	ATCDF5 J0033231.67-273415.5	03:32:31.67	-27:34:15.5	67	13	0	0	0.00	0.00	0.0	11.0

Table 2. continued

ID	IAU name	RA (J2000)	Dec (J2000)	S_{pnt} (μ Jy)	dS_{pnt} (μ Jy)	S_{int} (μ Jy)	dS_{int} (μ Jy)	Decon Bmajor	Decon Bminor	Decon PA	σ_{local}
71	ATCDF5 J0033231.54-275029.0	03:32:31.54	-27:50:29.0	103	10	0	0	0.00	0.00	0.0	9.2
72	ATCDF5 J0033230.56-275911.2	03:32:30.56	-27:59:11.2	117	8	187	33	5.04	0.89	11.2	7.9
73	ATCDF5 J0033230.00-274405.0	03:32:30.00	-27:44:05.0	109	9	174	21	2.73	1.51	42.4	9.0
74	ATCDF5 J0033229.86-274424.6	03:32:29.86	-27:44:24.6	193	10	381	43	4.44	1.85	-21.9	10.4
75	ATCDF5 J0033229.99-274302.3	03:32:29.99	-27:43:02.3	47	8	0	0	0.00	0.00	0.0	8.7
76A	ATCDF5 J0033229.57-274331.0	03:32:29.57	-27:43:31.0	63	13	228	85	5.43	4.41	4.8	12.7
76B	ATCDF5 J0033228.82-274355.8	03:32:28.82	-27:43:55.8	311	17	450	73	3.86	1.05	9.5	15.7
76C	ATCDF5 J0033228.68-274404.8	03:32:28.68	-27:44:04.8	164	15	1024	224	12.45	4.17	8.6	14.8
77	ATCDF5 J0033228.73-274620.6	03:32:28.73	-27:46:20.6	166	11	204	24	2.26	0.97	11.4	8.8
78	ATCDF5 J0033228.58-273536.6	03:32:28.58	-27:35:36.6	67	13	111	76	3.96	1.66	7.2	10.4
79	ATCDF5 J0033228.35-273841.8	03:32:28.35	-27:38:41.8	57	12	0	0	0.00	0.00	0.0	9.2
80A	ATCDF5 J0033227.34-274102.2	03:32:27.34	-27:41:02.2	191	12	397	69	4.31	2.42	2.9	10.6
80B	ATCDF5 J0033226.97-274107.0	03:32:26.97	-27:41:07.0	5114	150	7049	325	3.35	0.88	17.3	10.5
80C	ATCDF5 J0033226.57-274111.4	03:32:26.57	-27:41:11.4	68	10	138	79	4.48	1.99	-21.5	10.2
81	ATCDF5 J0033226.75-280454.9	03:32:26.75	-28:04:54.9	84	18	0	0	0.00	0.00	0.0	15.0
82	ATCDF5 J0033224.30-280114.5	03:32:24.30	-28:01:14.5	147	9	0	0	0.00	0.00	0.0	10.0
83	ATCDF5 J0033223.81-275845.1	03:32:23.81	-27:58:45.1	104	12	0	0	0.00	0.00	0.0	8.6
84	ATCDF5 J0033223.69-273648.3	03:32:23.69	-27:36:48.3	83	10	0	0	0.00	0.00	0.0	9.0
85	ATCDF5 J0033222.70-274127.2	03:32:22.70	-27:41:27.2	53	8	0	0	0.00	0.00	0.0	8.5
86	ATCDF5 J0033222.61-280023.9	03:32:22.61	-28:00:23.9	90	9	181	51	4.49	2.18	-7.1	9.2
87	ATCDF5 J0033222.52-274804.4	03:32:22.52	-27:48:04.4	55	6	0	0	0.00	0.00	0.0	8.3
88	ATCDF5 J0033221.72-280153.2	03:32:21.72	-28:01:53.2	93	6	0	0	0.00	0.00	0.0	9.9
89	ATCDF5 J0033221.28-274436.1	03:32:21.28	-27:44:36.1	87	10	0	0	0.00	0.00	0.0	9.3
90	ATCDF5 J0033221.07-273530.6	03:32:21.07	-27:35:30.6	102	10	0	0	0.00	0.00	0.0	10.5
91A	ATCDF5 J0033219.75-275401.3	03:32:19.75	-27:54:01.3	489	16	1003	72	3.64	2.22	42.2	11.4
91B	ATCDF5 J0033219.29-275406.2	03:32:19.29	-27:54:06.2	581	77	738	81	1.85	0.25	54.6	11.1
91C	ATCDF5 J0033219.10-275408.0	03:32:19.10	-27:54:08.0	545	41	875	102	2.98	0.83	49.6	10.9
91D	ATCDF5 J0033218.52-275412.2	03:32:18.52	-27:54:12.2	411	19	911	104	3.37	2.74	67.5	10.1
92	ATCDF5 J0033219.80-274123.2	03:32:19.80	-27:41:23.2	81	8	0	0	0.00	0.00	0.0	8.4
93	ATCDF5 J0033219.50-275218.1	03:32:19.50	-27:52:18.1	77	12	0	0	0.00	0.00	0.0	9.6
94	ATCDF5 J0033218.02-274718.6	03:32:18.02	-27:47:18.6	422	15	0	0	0.00	0.00	0.0	8.5
95	ATCDF5 J0033217.05-275846.6	03:32:17.05	-27:58:46.6	1718	13	0	0	0.00	0.00	0.0	10.0
96	ATCDF5 J0033217.04-275916.7	03:32:17.04	-27:59:16.7	50	11	88	31	3.41	2.05	10.8	8.8
97	ATCDF5 J0033215.95-273438.5	03:32:15.95	-27:34:38.5	217	15	258	38	2.03	0.91	2.3	10.8
98	ATCDF5 J0033215.39-273706.9	03:32:15.39	-27:37:06.9	58	8	0	0	0.00	0.00	0.0	9.3
99	ATCDF5 J0033214.83-275640.3	03:32:14.83	-27:56:40.3	82	10	0	0	0.00	0.00	0.0	8.8
100	ATCDF5 J0033213.89-275001.0	03:32:13.89	-27:50:01.0	92	11	0	0	0.00	0.00	0.0	8.4
101	ATCDF5 J0033213.48-274953.5	03:32:13.48	-27:49:53.5	90	12	0	0	0.00	0.00	0.0	8.7
102	ATCDF5 J0033213.23-274241.2	03:32:13.23	-27:42:41.2	44	12	0	0	0.00	0.00	0.0	8.2
103	ATCDF5 J0033213.08-274350.9	03:32:13.08	-27:43:50.9	283	11	424	29	2.42	1.79	-2.7	8.5
104	ATCDF5 J0033211.65-273726.2	03:32:11.65	-27:37:26.2	11886	70	0	0	0.00	0.00	0.0	13.0
105	ATCDF5 J0033211.53-274713.3	03:32:11.53	-27:47:13.3	90	8	0	0	0.00	0.00	0.0	8.5
106	ATCDF5 J0033211.50-274816.2	03:32:11.50	-27:48:16.2	50	12	0	0	0.00	0.00	0.0	8.8
107	ATCDF5 J0033210.92-274415.2	03:32:10.92	-27:44:15.2	2052	13	0	0	0.00	0.00	0.0	8.5
108	ATCDF5 J0033210.99-274053.8	03:32:10.99	-27:40:53.8	183	9	0	0	0.00	0.00	0.0	9.2
109	ATCDF5 J0033210.79-274628.1	03:32:10.79	-27:46:28.1	111	9	0	0	0.00	0.00	0.0	8.6
110	ATCDF5 J0033210.16-275938.4	03:32:10.16	-27:59:38.4	154	15	183	38	1.87	0.48	-32.1	9.9
111	ATCDF5 J0033209.81-275932.3	03:32:09.81	-27:59:32.3	67	10	0	0	0.00	0.00	0.0	9.9
112	ATCDF5 J0033209.71-274248.4	03:32:09.71	-27:42:48.4	517	11	0	0	0.00	0.00	0.0	8.8
113	ATCDF5 J0033208.67-274734.6	03:32:08.67	-27:47:34.6	3533	36	0	0	0.00	0.00	0.0	9.7
114	ATCDF5 J0033208.53-274649.0	03:32:08.53	-27:46:49.0	63	7	0	0	0.00	0.00	0.0	9.2
115	ATCDF5 J0033206.10-273235.7	03:32:06.10	-27:32:35.7	13803	114	0	0	0.00	0.00	0.0	20.0
116	ATCDF5 J0033204.68-280057.5	03:32:04.68	-28:00:57.5	73	15	0	0	0.00	0.00	0.0	9.3
117	ATCDF5 J0033204.31-280157.0	03:32:04.31	-28:01:57.0	61	10	0	0	0.00	0.00	0.0	9.8
118	ATCDF5 J0033203.88-275805.1	03:32:03.88	-27:58:05.1	111	9	0	0	0.00	0.00	0.0	8.5
119	ATCDF5 J0033203.67-274603.9	03:32:03.67	-27:46:03.9	60	9	0	0	0.00	0.00	0.0	8.7
120	ATCDF5 J0033202.84-275613.2	03:32:02.84	-27:56:13.2	63	8	0	0	0.00	0.00	0.0	7.5
121A	ATCDF5 J0033201.56-274647.8	03:32:01.56	-27:46:47.8	4910	178	6763	437	2.12	0.93	51.3	10.1
121B	ATCDF5 J0033201.28-274647.7	03:32:01.28	-27:46:47.7	3576	192	4489	477	2.25	0.66	30.9	10.3
122	ATCDF5 J0033200.84-273557.0	03:32:00.84	-27:35:57.0	2417	22	0	0	0.00	0.00	0.0	9.5
123	ATCDF5 J0033159.83-274540.7	03:31:59.83	-27:45:40.7	81	9	0	0	0.00	0.00	0.0	8.3
124	ATCDF5 J0033158.93-274359.4	03:31:58.93	-27:43:59.4	51	7	0	0	0.00	0.00	0.0	8.4
125	ATCDF5 J0033158.33-273747.9	03:31:58.33	-27:37:47.9	49	6	0	0	0.00	0.00	0.0	8.8
126	ATCDF5 J0033157.75-274208.9	03:31:57.75	-27:42:08.9	54	6	0	0	0.00	0.00	0.0	8.0
127	ATCDF5 J0033155.00-274410.7	03:31:55.00	-27:44:10.7	75	9	0	0	0.00	0.00	0.0	8.8
128	ATCDF5 J0033154.88-275341.0	03:31:54.88	-27:53:41.0	51	10	0	0	0.00	0.00	0.0	8.0
129	ATCDF5 J0033153.42-280221.3	03:31:53.42	-28:02:21.3	665	12	0	0	0.00	0.00	0.0	10.5
130	ATCDF5 J0033152.12-273926.5	03:31:52.12	-27:39:26.5	558	12	0	0	0.00	0.00	0.0	8.7
131	ATCDF5 J0033151.31-275056.0	03:31:51.31	-27:50:56.0	52	8	0	0	0.00	0.00	0.0	8.0
132	ATCDF5 J0033150.78-274703.9	03:31:50.78	-27:47:03.9	110	6	0	0	0.00	0.00	0.0	8.4
133	ATCDF5 J0033150.13-273948.3	03:31:50.13	-27:39:48.3	243	18	333	83	3.32	1.03	10.3	9.6
134	ATCDF5 J0033150.02-275806.3	03:31:50.02	-27:58:06.3	173	10	0	0	0.00	0.00	0.0	8.6
135	ATCDF5 J0033149.88-274839.0	03:31:49.88	-27:48:39.0	850	35	1173	82	1.81	1.15	77.3	8.7
136	ATCDF5 J0033148.74-273311.9	03:31:48.74	-27:33:11.9	90	10	0	0	0.00	0.00	0.0	12.5
137	ATCDF5 J0033147.38-274542.2	03:31:47.38	-27:45:42.2	121	9	147	24	2.99	0.49	-7.0	8.6
138	ATCDF5 J0033146.58-275734.6	03:31:46.58	-27:57:34.6	155	17	188	47	2.53	0.53	19.3	8.3
139	ATCDF5 J0033146.09-280026.5	03:31:46.09	-28:00:26.5	186	10	0	0	0.00	0.00	0.0	8.7
140	ATCDF5 J0033145.91-274539.1	03:31:45.91	-27:45:39.1	55	10	0	0	0.00	0.00	0.0	9.3

Table 2. continued

ID	IAU name	RA (J2000)	Dec (J2000)	S_{pnt} (μ Jy)	dS_{pnt} (μ Jy)	S_{int} (μ Jy)	dS_{int} (μ Jy)	Decon Bmajor	Decon Bminor	Decon PA	σ_{local}
141	ATCDF5 J0033144.02-273836.2	03:31:44.02	-27:38:36.2	79	9	0	0	0.00	0.00	0.0	8.2
142	ATCDF5 J0033143.34-275102.6	03:31:43.34	-27:51:02.6	54	12	0	0	0.00	0.00	0.0	8.4
143	ATCDF5 J0033143.42-274248.7	03:31:43.42	-27:42:48.7	38	7	0	0	0.00	0.00	0.0	7.9
144	ATCDF5 J0033143.22-275405.5	03:31:43.22	-27:54:05.5	52	5	0	0	0.00	0.00	0.0	8.5
145	ATCDF5 J0033140.05-273648.1	03:31:40.05	-27:36:48.1	91	16	0	0	0.00	0.00	0.0	9.2
146	ATCDF5 J0033139.54-274120.1	03:31:39.54	-27:41:20.1	71	9	0	0	0.00	0.00	0.0	8.4
147	ATCDF5 J0033139.04-275259.1	03:31:39.04	-27:52:59.1	53	7	0	0	0.00	0.00	0.0	8.6
148	ATCDF5 J0033138.47-275942.1	03:31:38.47	-27:59:42.1	71	8	0	0	0.00	0.00	0.0	8.7
149	ATCDF5 J0033137.79-280533.6	03:31:37.79	-28:05:33.6	109	17	0	0	0.00	0.00	0.0	17.2
150	ATCDF5 J0033136.09-273940.8	03:31:36.09	-27:39:40.8	58	10	0	0	0.00	0.00	0.0	8.5
151	ATCDF5 J0033135.20-273508.9	03:31:35.20	-27:35:08.9	53	6	0	0	0.00	0.00	0.0	9.3
152	ATCDF5 J0033134.22-273828.7	03:31:34.22	-27:38:28.7	268	16	0	0	0.00	0.00	0.0	9.0
153	ATCDF5 J0033132.81-280116.2	03:31:32.81	-28:01:16.2	58	9	0	0	0.00	0.00	0.0	9.5
154A	ATCDF5 J0033131.08-273815.8	03:31:31.08	-27:38:15.8	1792	83	3133	234	2.63	1.72	-77.0	11.7
154B	ATCDF5 J0033130.01-273814.0	03:31:30.01	-27:38:14.0	219	24	303	63	1.72	1.60	-55.1	13.0
154C	ATCDF5 J0033129.58-273802.9	03:31:29.58	-27:38:02.9	200	13	450	62	4.24	2.64	-20.1	12.5
155	ATCDF5 J0033130.74-275734.9	03:31:30.74	-27:57:34.9	196	9	0	0	0.00	0.00	0.0	8.4
156A	ATCDF5 J0033130.38-275606.0	03:31:30.38	-27:56:06.0	90	11	237	52	4.94	3.14	7.9	10.7
156B	ATCDF5 J0033130.05-275602.8	03:31:30.05	-27:56:02.8	105	11	152	44	3.58	1.00	-15.1	10.9
156C	ATCDF5 J0033129.81-275559.7	03:31:29.81	-27:55:59.7	65	11	167	98	5.47	2.81	0.0	10.8
157	ATCDF5 J0033129.90-275722.7	03:31:29.90	-27:57:22.7	56	10	0	0	0.00	0.00	0.0	8.8
158	ATCDF5 J0033129.77-273218.4	03:31:29.77	-27:32:18.4	1735	23	0	0	0.00	0.00	0.0	18.1
159	ATCDF5 J0033128.59-274935.0	03:31:28.59	-27:49:35.0	180	8	0	0	0.00	0.00	0.0	8.9
160	ATCDF5 J0033127.57-274439.1	03:31:27.57	-27:44:39.1	56	10	0	0	0.00	0.00	0.0	9.5
161	ATCDF5 J0033127.20-274247.2	03:31:27.20	-27:42:47.2	584	13	667	26	2.23	0.52	-8.2	8.6
162	ATCDF5 J0033127.04-275958.2	03:31:27.04	-27:59:58.2	135	13	0	0	0.00	0.00	0.0	9.7
163	ATCDF5 J0033127.06-274409.7	03:31:27.06	-27:44:09.7	173	8	0	0	0.00	0.00	0.0	9.3
164	ATCDF5 J0033126.78-274237.1	03:31:26.78	-27:42:37.1	108	13	137	37	2.94	0.90	-2.6	8.8
165	ATCDF5 J0033125.27-275958.6	03:31:25.27	-27:59:58.6	85	9	0	0	0.00	0.00	0.0	9.8
166	ATCDF5 J0033124.90-275208.0	03:31:24.90	-27:52:08.0	6454	205	12243	648	3.48	1.01	59.6	12.3
167	ATCDF5 J0033124.63-280454.3	03:31:24.63	-28:04:54.3	103	14	0	0	0.00	0.00	0.0	18.4
168	ATCDF5 J0033123.30-274905.8	03:31:23.30	-27:49:05.8	547	14	559	29	0.99	0.15	2.5	9.2
169	ATCDF5 J0033123.07-275430.0	03:31:23.07	-27:54:30.0	58	14	0	0	0.00	0.00	0.0	10.1
170	ATCDF5 J0033122.21-275755.1	03:31:22.21	-27:57:55.1	44	8	0	0	0.00	0.00	0.0	9.0
171	ATCDF5 J0033121.85-275445.4	03:31:21.85	-27:54:45.4	78	10	0	0	0.00	0.00	0.0	9.9
172	ATCDF5 J0033120.21-280146.7	03:31:20.21	-28:01:46.7	81	15	154	69	2.95	2.57	6.0	13.3
173	ATCDF5 J0033120.15-273901.1	03:31:20.15	-27:39:01.1	112	11	0	0	0.00	0.00	0.0	10.2
174	ATCDF5 J0033119.90-273549.9	03:31:19.90	-27:35:49.9	67	10	0	0	0.00	0.00	0.0	12.2
175	ATCDF5 J0033118.73-274902.2	03:31:18.73	-27:49:02.2	117	11	0	0	0.00	0.00	0.0	10.7
176	ATCDF5 J0033117.34-280147.3	03:31:17.34	-28:01:47.3	458	15	491	28	1.17	0.59	5.5	13.7
177A	ATCDF5 J0033117.04-275515.3	03:31:17.04	-27:55:15.3	479	26	959	91	4.49	2.03	-14.0	12.0
177B	ATCDF5 J0033115.04-275518.7	03:31:15.04	-27:55:18.7	1551	20	0	0	0.00	0.00	0.0	14.1
177C	ATCDF5 J0033114.36-275519.7	03:31:14.36	-27:55:19.7	163	14	483	89	5.36	2.74	49.6	14.0
177D	ATCDF5 J0033113.93-275519.7	03:31:13.93	-27:55:19.7	619	17	1857	149	5.42	1.99	68.2	13.8
178	ATCDF5 J0033115.99-274443.1	03:31:15.99	-27:44:43.1	357	17	412	42	2.21	0.67	2.4	12.0
179	ATCDF5 J0033114.46-275546.6	03:31:14.46	-27:55:46.6	117	18	0	0	0.00	0.00	0.0	12.7
180	ATCDF5 J0033114.51-273906.6	03:31:14.51	-27:39:06.6	71	14	0	0	0.00	0.00	0.0	12.1
181	ATCDF5 J0033113.95-273910.4	03:31:13.95	-27:39:10.4	533	24	0	0	0.00	0.00	0.0	12.7
182	ATCDF5 J0033112.58-275717.9	03:31:12.58	-27:57:17.9	235	10	0	0	0.00	0.00	0.0	12.0
183	ATCDF5 J0033111.80-275817.3	03:31:11.80	-27:58:17.3	69	17	0	0	0.00	0.00	0.0	13.6
184	ATCDF5 J0033111.50-275258.5	03:31:11.50	-27:52:58.5	91	16	0	0	0.00	0.00	0.0	14.5
185	ATCDF5 J0033109.81-275225.3	03:31:09.81	-27:52:25.3	652	21	0	0	0.00	0.00	0.0	15.6
186	ATCDF5 J0033109.94-274915.8	03:31:09.94	-27:49:15.8	68	14	144	25	6.02	1.84	-1.3	13.0
187	ATCDF5 J0033109.18-274954.5	03:31:09.18	-27:49:54.5	140	18	0	0	0.00	0.00	0.0	14.3
188	ATCDF5 J0033107.97-275047.6	03:31:07.97	-27:50:47.6	78	15	0	0	0.00	0.00	0.0	15.2
189	ATCDF5 J0033106.15-273837.7	03:31:06.15	-27:38:37.7	142	14	0	0	0.00	0.00	0.0	16.8

(52 μ Jy), as determined by the simulations of Section 3.4, to be σ_{det} . The minimum angular size (θ_{min}) is estimated from Equation 1, with σ equal to the typical noise of the full image (8.4 μ Jy).

The angular sizes (θ) of the catalogued sources as a function of total flux density is shown in Figure 8, where the angular size θ is defined as the geometric mean of the fitted Gaussian major and minor axes. We find that the largest catalogued sources are in good agreement with the θ_{max} function. The θ_{min} constraint is important at low flux density levels, where θ_{max} becomes unphysical (smaller than a point source). Also shown in Figure 8 (dashed lines) is the expected median angular size obtained from Windhorst et al. (1990) for a 1.4 GHz sample, $\theta_{med} = 2'' S_{1.4GHz}^{0.30}$, where $S_{1.4GHz}$ is in mJy. We extrapolated to 5.5 GHz assuming a

spectral index of 0, -0.5 and -0.8 between 1.4 and 5.5 GHz. At the bright end ($S > 2$ mJy) our source sizes are consistent with the Windhorst et al. (1990) relation, however most of the sources are unresolved and therefore we can not draw any conclusions about the full sample.

The overall angular size limit, $\theta_{lim} = \max(\theta_{max}, \theta_{min})$, and an expected integral size distribution, $h(\theta)$, allows an estimation of the fraction of sources larger than the maximum detectable size, and hence missed by the survey. The resolution bias correction factor is then simply $\frac{1}{1-h(\theta)}$. The correction factor for Windhorst et al. (1990) and Muxlow et al. (2005) integral size distributions are shown in Figure 8. The resolution bias correction for the Windhorst et al. (1990) integral size distribution has a maximum of about 1.3 at a flux density of 70–80 μ Jy. The Windhorst et al. (1990)

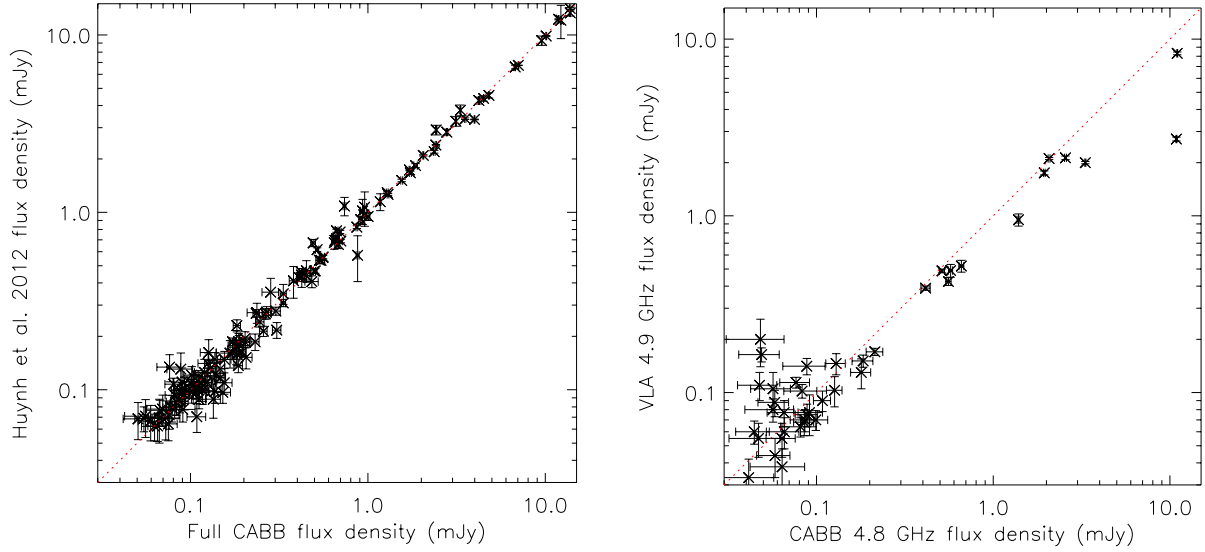


Figure 5. LEFT: Comparison of the flux densities in this data release using the full band reduction (i.e. flux densities from Table 2) compared to Data Release 1 (H12). The sources lie close to the dotted line, which shows that flux densities in this data release are consistent with those measured in Data Release 1 (H12). RIGHT: The 4.8 GHz sub-band flux density versus the 4.9 GHz VLA flux density, for sources with a VLA measurement.

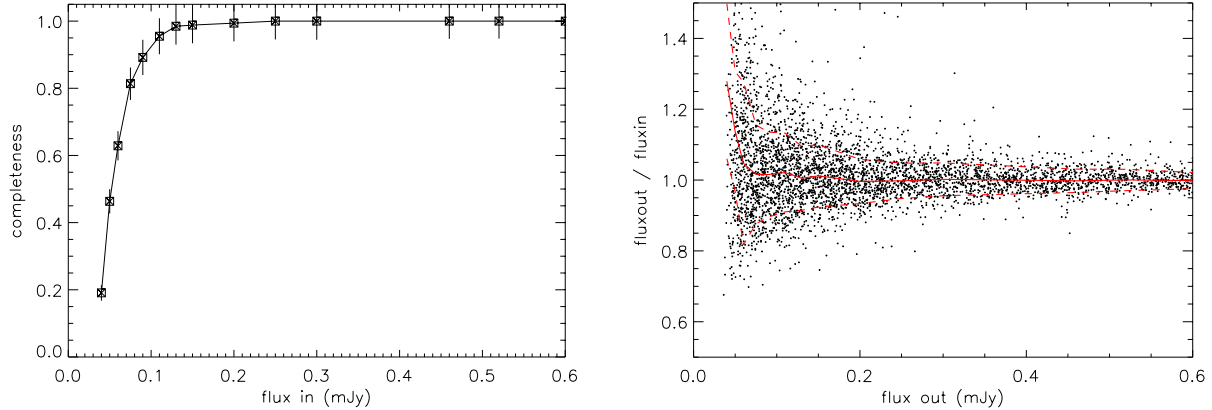


Figure 6. LEFT: Completeness as a function of input flux density, as derived from the Monte-Carlo simulations. Completeness is the number of extracted sources divided by number of input sources. RIGHT: The distribution of output/input flux density as a function of output flux density for the simulated sources. The solid red line is the median of the simulation and the dashed lines mark the 1 sigma upper and lower bounds. The effect of flux boosting at the faint end is dramatically illustrated by the rapid upturn below about 0.075 mJy.

integral size distribution is commonly used to determine resolution bias (e.g. Prandoni et al. 2001) so we include it in our source count derivation, but we note it is derived from a brighter sample than our work ($S_{1.4\text{GHz}} > 0.4$ mJy). The Muxlow et al. (2005) sample goes to sub-100- μJy levels, but it comes from high resolution MERLIN and VLA imaging which may miss low surface brightness galaxies. We note that the resolution bias is negligible if the Muxlow et al. (2005) size distribution is assumed.

4 SOURCE COUNTS

The differential radio source counts were constructed from the catalogue of Section 3. Integrated flux densities were used for resolved sources, and components of multiple

sources were summed and counted as a single source. The results are summarised in Table 3, where for each bin we report the flux density interval, mean flux density, the number of sources detected (N), the number of sources after completeness, flux boosting and resolution bias corrections have been applied (N_C), the differential source count (dN_C/dS), and the normalised counts (N_C/N_{exp}). The counts are normalised to N_{exp} , the number expected in the bin from the standard Euclidean count, for comparison with counts in the literature. At 6cm the standard Euclidean integral counts are $N(> S_{6\text{cm}}) = 60 \times S_{6\text{cm}}^{-1.5} \text{ sr}^{-1}$, where $S_{6\text{cm}}$ is in Jy (Donnelly et al. 1987; Fomalont et al. 1991; Ciliegi et al. 2003). The Poissonian errors in the count are $CN^{1/2}/N_{\text{exp}}$, where C is the total correction factor, N_C/N . The estimated total uncertainty in the counts is the Poissonian error with the resolution bias uncertainty (10%), the flux boosting uncer-

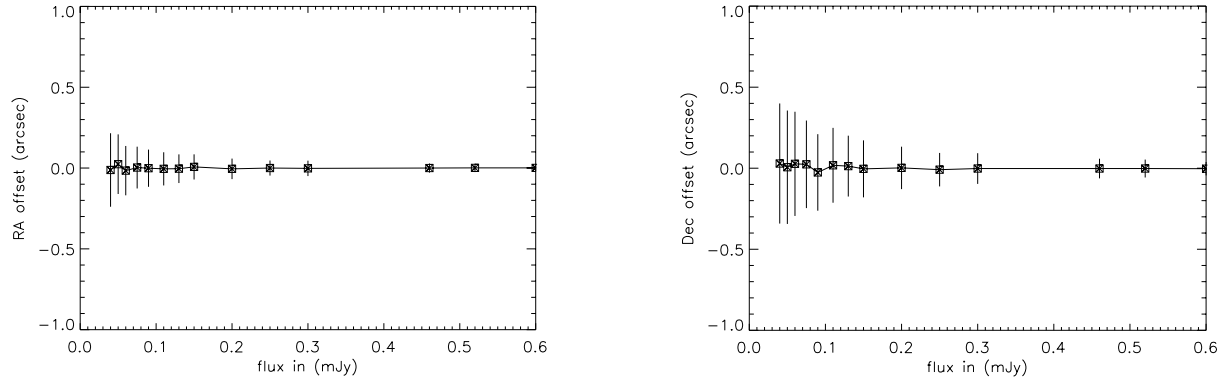


Figure 7. LEFT: The offset in RA between the recovered positions of sources in the simulation and the true input positions, as a function of input flux density. The error bars mark the 1 sigma uncertainty in the position as a function of input flux density. RIGHT: Same as the left panel, but for offset in Dec.

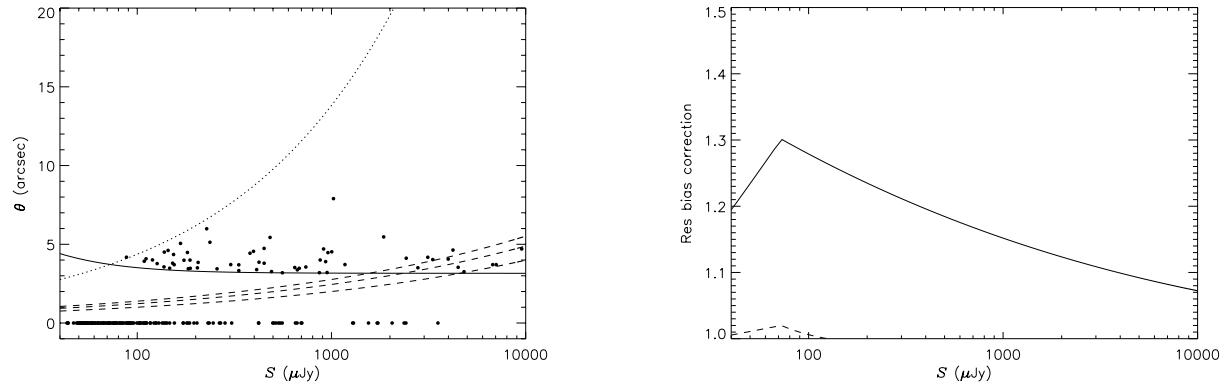


Figure 8. LEFT: The fitted angular size as a function of total flux density. Point sources are shown with an angular size of zero. The solid line indicates the minimum angular size (θ_{\min}) of sources in the survey, below which deconvolution is not considered meaningful. The dotted line shows the maximum angular size (θ_{\max}) above which the survey becomes incomplete due to resolution bias. The dashed lines indicate the median source sizes expected from the Windhorst et al. (1990) relation, as a function of flux density, for a spectral index of 0, -0.5 and -0.8 between 1.4 and 5.5 GHz. RIGHT: The resolution bias correction as a function of flux density, assuming the Windhorst et al. (1990) integral angular source size distribution (solid line) and assuming the Muxlow et al. (2005) size distribution (dashed line).

tainty (5 – 20 %), and completeness correction uncertainty (2 – 4 %) all added in quadrature.

Our results are compared with previous work in Figure 9. Our source counts are consistent with the ATESP 6cm source counts (Prandoni et al. 2006) for $S_{6\text{cm}} > 0.4$ mJy. At fainter flux densities our counts hint at a flattening of the differential source counts, with a slope of $\alpha = 0.32 \pm 0.19$ for $\log(N_C/N_{\text{exp}}) \propto \log(S_{6\text{cm}})^\alpha$ at $S_{6\text{cm}} < 0.4$ mJy compared to $\alpha = 0.51 \pm 0.35$ at $S_{6\text{cm}} > 0.4$ mJy, but the difference in α is not statistically significant. Our source counts are lower than the Ciliegi et al. (2003) counts but consistent within the uncertainties, except for the faintest two bins. The counts in our faintest bins ($40 < S < 80 \mu\text{Jy}$) are about a factor of two lower than the Ciliegi et al. (2003) and Fomalont et al. (1991) counts at similar flux densities. Fomalont et al. (1991) catalogued sources to about 4σ in their image, so it is likely that they have spurious sources in their faintest bins. We note that our survey area is 4 times greater than Ciliegi et al. (2003) (0.34 deg^2 versus 0.087 deg^2) and 7 times greater than Fomalont et al. (1991) (0.34 deg^2 versus 0.05 deg^2). Most of the difference in the counts at the faint end can be attributed to cosmic variance and clustering (e.g.

H12, Heywood et al. 2013). The 6cm surveys in the literature have a central frequency of 5 GHz and the difference of 0.5 GHz in the central observing frequency may have an impact on the source count comparison. If a spectral index of -0.8 is applied to convert our 5.5 GHz flux densities to 5 GHz ones than the source counts change by at most 6% for $S_{6\text{cm}} < 0.1$ mJy, and hence the different central frequency does not account for the difference in our source counts compared to previous 6cm surveys in the faintest bins.

We also compare the observed source counts to the simulations of Wilman et al. (2008, 2010) in Figure 9. Briefly, this is a semi-empirical extragalactic simulation which uses observed and extrapolated luminosity functions of various radio populations (radio loud AGN split into FRI and FRII classes, radio quiet AGN, ‘normal’ starforming galaxies and starbursts) and places them on top of a dark matter density field with biases to reflect their observed large-scale clustering properties. This simulation (known as SKADS S-cubed¹) covers a sky area of 20×20 degrees and comprises 320 mil-

¹ <http://s-cubed.physics.ox.ac.uk>

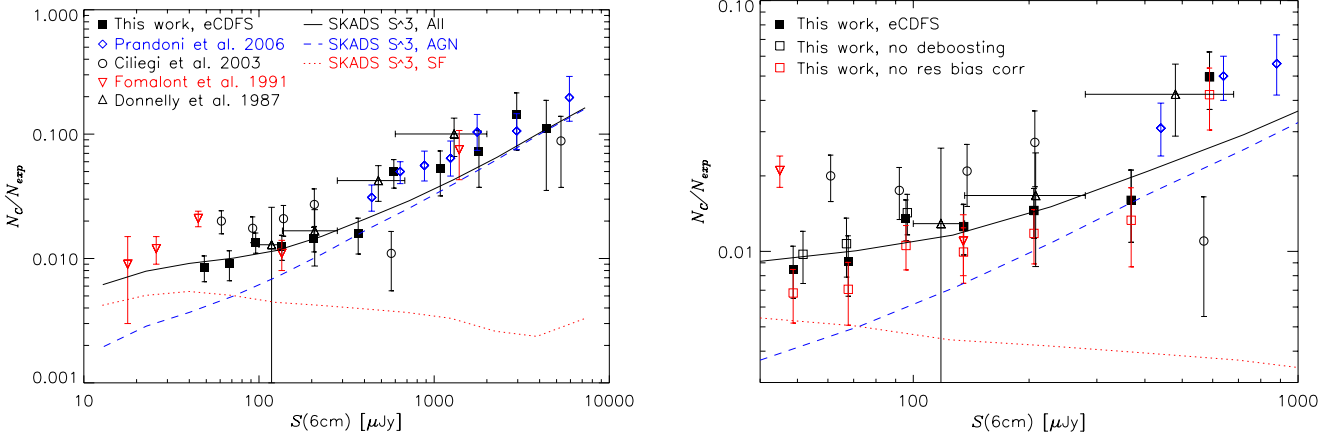


Figure 9. LEFT: Normalized 5.5 GHz differential source counts for different samples: Prandoni et al. (2006) (blue diamonds); Ciliegi et al. (2003) (empty circles); Fomalont et al. (1991) (red upside-down triangles); Donnelly et al. (1987) (empty triangles). The eCDFS 5.5 GHz source counts presented in this work (filled squares) are corrected for completeness, flux boosting and resolution bias as explained in the text. Vertical bars represent Poisson errors on the normalized counts. RIGHT: A zoom of the source counts in the 0.040 to 1 mJy flux density range, showing the effect of the different corrections. Black empty squares are the counts without the flux boosting correction. Red empty squares are counts without resolution bias correction. Other symbols are as for the left figure.

Table 3. The 5.5 GHz source counts.

ΔS (μJy)	$\langle S \rangle$ (μJy)	N	N_C	dN_C/dS ($\text{sr}^{-1} \text{Jy}^{-1}$)	N_C/N_{exp} ($\times 10^{-2}$)
40 – 57	49	33	78.8	4.61×10^{10}	0.85 ± 0.20
57 – 80	68	30	52.3	2.16×10^{10}	0.91 ± 0.25
80 – 113	96	33	46.3	1.36×10^{10}	1.35 ± 0.25
113 – 159	135	20	25.6	5.31×10^9	1.25 ± 0.29
159 – 270	206	20	24.8	2.15×10^9	1.46 ± 0.33
270 – 459	368	9	10.8	5.52×10^8	1.60 ± 0.51
459 – 780	589	15	17.7	5.31×10^8	4.96 ± 1.28
780 – 1325	1084	6	6.9	1.22×10^8	5.25 ± 2.07
1325 – 2249	1802	4	4.5	4.70×10^7	7.20 ± 3.47
2249 – 3820	2960	4	4.4	2.73×10^7	14.45 ± 7.01
3820 – 6487	4367	2	2.2	7.93×10^6	11.11 ± 7.58

lion sources to the flux density limit of 10 nJy. In general the modelled 4.86 GHz source counts are in good agreement with the observed counts, and this is remarkable given the level of complexity in the simulation. However the model counts in the ~ 0.5 –2 mJy flux density range underestimate the number of observed sources by 0.2 to 0.3 dex. FRIs dominate the model count at this flux density level so it is possible that either the FRIs are modelled incorrectly, i.e. jet Lorentz factors or radio lobe ratios used in the models are not correct for sources in this flux density range, or a population is missing from the simulations. A flat spectrum population detected at higher frequencies (> 10 GHz) but missing from 1.4 GHz surveys was recently identified (Whitlam et al. 2013; Franzen et al. 2014) and this small excess in the 5.5 GHz counts at \sim mJy levels is consistent with this discovery.

5 RADIO SPECTRAL ENERGY DISTRIBUTIONS

5.1 1.4 to 5.5 GHz Spectral Indices

To study the spectral index properties of the faint radio population we matched the 5.5 GHz catalogue to sources in the second data release of the VLA 1.4 GHz survey of the eCDFS (Miller et al. 2013). This improves on the initial VLA data with a $0.5 \mu\text{Jy}/\text{beam}$ rms noise reduction across the VLA mosaic to typical values of $7.4 \mu\text{Jy}/\text{beam}$ rms (i.e. $\sim 7\%$ improvement), and a deeper source catalogue detection limit of 5σ versus 7σ in the initial release. VLA imaging of the eCDFS has similar coverage to our observations, roughly $34' \times 34'$. Importantly, the beam of the VLA observations is $2.8'' \times 1.6''$ beam, which is only a factor of ~ 1.5 smaller than our observations. With similar resolution and sensitivity these images have a similar surface brightness sensitivity, and thus the measured flux densities can be used directly for spectral index analyses.

Multi-component sources were removed from the spectral index analysis as their interpretation is complicated by the core-jet structure, resulting in 177 individual 5.5 GHz sources for investigation. 163/177 (92%) of the 5.5 GHz sources have a 1.4 GHz match within 2 arcsec (FWHM of the synthesised beam of the VLA observations). The unmatched 5.5 GHz sources were inspected and four had counterparts in the 1.4 GHz image but weren't in the Miller et al. (2013) catalogue. The 1.4 GHz flux density for these sources was measured manually with the MIRIAD task *imfit*. In summary 167/177 (94%) of the 5.5 GHz sources in the 1.4 GHz image area have a 1.4 GHz counterpart, and hence a spectral index measurement (Table 4). Of the remaining 10 sources, 2 show multi-component source structure in the VLA image and 7 are faint at 5.5 GHz or located at the higher noise edges of the mosaic, indicating they are possibly spurious sources.

The median spectral index of this 5.5 GHz selected sample is $\alpha_{\text{med}} = -0.58$ (see Figure 10) and $\alpha_{\text{mean}} = -0.47 \pm 0.04$. This median spectral index is marginally steeper than

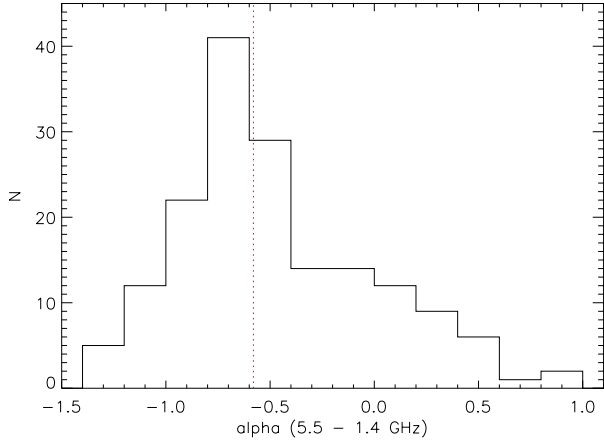


Figure 10. Spectral index distribution for sources in the ATCA 6cm sample. The vertical dotted line indicates the median value of the sample ($\alpha_{med} = -0.58$).

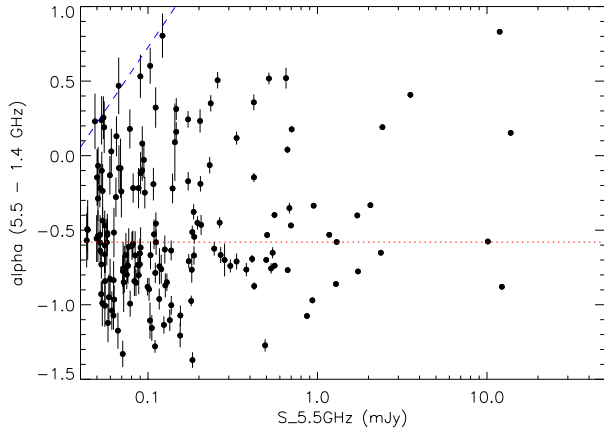


Figure 11. The 5.5–1.4 GHz spectral index vs. 5.5 GHz flux density for the ATCA 5.5 GHz selected sample. Only single component sources are shown. The dotted line indicates the median spectral index, $\alpha = -0.58$. The dashed line shows the 5σ limit of the VLA 1.4 GHz observations, showing this sample is sensitive to inverted sources at the faintest 5.5 GHz levels.

our previous work which found $\alpha_{med} = -0.40$ (H12). Figure 11 presents the spectral index as a function of 5.5 GHz flux density, and it shows that a population of steep spectrum sources at $S_{5.5GHz} < 0.1$ mJy is responsible for the slightly steeper average spectral index compared to earlier work in H12. This indicates that these new deeper observations may be starting to probe the star forming population. However, even at these low flux densities a significant fraction (31/79, 39%) of the 5.5 GHz sample has a flat or inverted spectral index ($\alpha > -0.5$). For $S_{5.5GHz} > 0.5$ mJy the median spectral index is $\alpha_{med} = -0.47$ and the average spectral index is $\alpha_{mean} = -0.35 \pm 0.10$, which is consistent with published values for 6cm selected sources of similar flux density. For example Prandoni et al. (2006) found $\alpha_{med} = -0.4$ for $0.4 < S_{5GHz} < 4$ mJy and Donnelly et al. (1987) who found $\alpha_{med} = -0.42$ for $0.4 < S_{5GHz} < 1.2$ mJy.

Table 4. The 1.4 – 5.5 GHz spectral index of the ATCA 5.5 GHz sample.

ID	$S_{5.5GHz}$ (μ Jy)	$S_{1.4GHz}$ (μ Jy)	α	$\delta\alpha$
1	283	729.0	-0.70	0.11
2	306	831.0	-0.74	0.04
3	544	1310.0	-0.65	0.04
4	155	660.0	-1.07	0.07
5	505	1036.0	-0.53	0.02
6	96	133.9	-0.25	0.11
7	95	98.3	-0.03	0.12
8	421	260.0	0.36	0.05
9	155	789.8	-1.21	0.08
10	231	252.0	-0.06	0.05
11	93	83.0	0.08	0.12
12	265	485.6	-0.45	0.04
13	56	136.1	-0.66	0.13
14	72	226.3	-0.85	0.20
15	76	204.6	-0.74	0.11
16	108	139.4	-0.19	0.11
17	120	334.9	-0.76	0.10
18	1286	4108.0	-0.86	0.01
19	697	1312.0	-0.47	0.01
21	1298	2836.0	-0.58	0.01
22	704	554.6	0.18	0.02
23	246	571.1	-0.62	0.05
24	137	323.6	-0.64	0.07
25	67	35.7	0.47	0.19
26	100	326.2	-0.88	0.06
27	10114	22000.0	-0.58	0.00
28	127	410.0	-0.87	0.08
29	499	1281.0	-0.70	0.01
30	51	104.9	-0.54	0.17
31	63	193.7	-0.84	0.13
32	333	284.3	0.12	0.04
33	61	248.8	-1.04	0.13
34	65	54.7	0.13	0.13
35	49	35.7	0.23	0.19
36	60	182.6	-0.83	0.14
37	63	126.4	-0.52	0.17
39	949	1493.0	-0.34	0.01
40	122	41.1	0.80	0.15
41	683	1098.0	-0.35	0.04
42	52	123.8	-0.64	0.11
43	65	94.2	-0.28	0.13
44	203	148.3	0.23	0.08
45	70	96.4	-0.24	0.17
47	206	385.1	-0.46	0.07
48	59	211.9	-0.95	0.15
49	867	3700.0	-1.08	0.01
50	2366	5697.0	-0.65	0.01
51	109	221.4	-0.53	0.10
52	44	93.7	-0.57	0.18
53	76	206.8	-0.74	0.12
54	50	105.5	-0.56	0.16
56	933	3458.0	-0.97	0.02
57	126	294.0	-0.63	0.09
58	88	260.5	-0.80	0.13
60	74	182.1	-0.67	0.15
61	129	406.8	-0.85	0.06
62	124	575.2	-1.14	0.06
63	53	185.7	-0.93	0.09
64	52	107.0	-0.53	0.13
65	56	173.9	-0.84	0.18
66	56	104.5	-0.47	0.10
67	54	204.4	-0.99	0.16
68	105	501.8	-1.16	0.09

Table 4. continued

ID	$S_{5.5GHz}$ (μ Jy)	$S_{1.4GHz}$ (μ Jy)	α	$\delta\alpha$
70	67	75.4	-0.08	0.15
71	103	45.7	0.60	0.12
72	187	461.5	-0.67	0.06
73	174	452.2	-0.71	0.05
74	381	1068.0	-0.76	0.04
77	204	263.3	-0.19	0.05
78	111	71.8	0.32	0.14
79	57	125.4	-0.58	0.15
81	84	207.2	-0.67	0.16
82	147	118.3	0.16	0.06
83	104	254.9	-0.67	0.09
84	83	258.9	-0.84	0.10
85	53	38.7	0.24	0.16
86	181	509.4	-0.77	0.09
87	55	38.7	0.25	0.14
88	93	105.7	-0.10	0.07
89	87	234.2	-0.73	0.09
90	102	340.2	-0.90	0.08
92	81	180.9	-0.59	0.09
93	77	175.7	-0.61	0.12
94	422	513.6	-0.15	0.03
95	1718	2952.0	-0.40	0.01
96	88	118.1	-0.22	0.14
97	258	130.1	0.51	0.06
98	58	117.9	-0.53	0.11
99	82	109.7	-0.22	0.10
101	90	44.0	0.53	0.15
102	44	86.4	-0.50	0.20
103	424	1380.0	-0.88	0.03
104	11886	3871.0	0.83	0.00
105	90	239.3	-0.73	0.08
106	50	61.0	-0.15	0.19
107	2052	3213.0	-0.33	0.01
108	183	364.9	-0.51	0.04
109	111	206.0	-0.46	0.08
110	183	1165.0	-1.37	0.05
112	517	257.2	0.52	0.04
113	3533	2037.0	0.41	0.01
114	63	232.5	-0.96	0.09
115	13803	11230.0	0.15	0.01
116	73	202.7	-0.76	0.16
117	61	58.5	0.03	0.15
118	111	319.5	-0.79	0.07
119	60	71.2	-0.13	0.13
120	63	266.2	-1.07	0.10
122	2417	1868.0	0.19	0.01
123	81	182.1	-0.60	0.09
124	51	55.7	-0.07	0.13
126	54	97.2	-0.44	0.09
127	75	220.3	-0.80	0.10
128	51	74.7	-0.29	0.15
129	665	630.3	0.04	0.02
130	558	954.2	-0.40	0.02
131	52	69.8	-0.22	0.13
132	110	619.0	-1.28	0.04
133	333	868.8	-0.71	0.05
134	173	217.5	-0.17	0.06
135	1173	2402.0	-0.53	0.01
136	90	217.2	-0.66	0.10
137	147	96.3	0.31	0.07
138	188	391.0	-0.54	0.05
139	186	309.5	-0.38	0.05
140	55	42.7	0.19	0.17
141	79	299.8	-0.99	0.09
142	54	74.3	-0.24	0.18

Table 4. continued

ID	$S_{5.5GHz}$ (μ Jy)	$S_{1.4GHz}$ (μ Jy)	α	$\delta\alpha$
143	38	75.4	-0.52	0.15
144	52	115.0	-0.58	0.09
145	91	208.1	-0.62	0.14
146	71	202.6	-0.77	0.11
147	53	61.2	-0.10	0.13
148	71	427.6	-1.33	0.09
150	58	116.1	-0.52	0.13
151	53	142.1	-0.73	0.10
152	268	659.7	-0.67	0.05
153	58	264.2	-1.12	0.13
155	196	360.0	-0.45	0.04
157	56	125.3	-0.60	0.14
158	1735	4950.0	-0.78	0.01
159	180	670.8	-0.97	0.04
160	56	216.7	-1.01	0.14
161	667	1880.0	-0.77	0.01
162	135	596.4	-1.10	0.07
163	173	124.2	0.24	0.06
164	137	531.9	-1.00	0.06
165	85	268.5	-0.85	0.09
166	12243	40130.0	-0.88	0.00
167	103	457.5	-1.11	0.12
168	559	1513.0	-0.74	0.01
170	44	85.4	-0.49	0.15
171	78	61.4	0.18	0.13
173	112	244.7	-0.58	0.08
174	67	324.3	-1.17	0.12
175	117	427.1	-0.96	0.07
176	491	2736.0	-1.27	0.04
178	412	1049.0	-0.69	0.03
179	117	318.3	-0.74	0.12
180	71	198.1	-0.76	0.18
181	533	1479.0	-0.76	0.03
182	235	146.1	0.35	0.06
183	69	77.2	-0.08	0.20
184	91	105.9	-0.12	0.14
185	652	325.0	0.52	0.07
186	144	128.0	0.09	0.26
187	140	189.0	-0.22	0.10

5.2 Radio Spectral Curvature

The 4 sub-bands across the full 2 GHz band at 6cm provide us with the opportunity to study in more detail the radio spectral energy distribution (SED) of our sources. The radio SED of galaxies can be complex and is not always well described by a power law. Self-synchrotron absorption leads to a turnover at low frequencies ($\nu_{rest} \ll 1$ GHz) but for young compact AGN the turnover frequency can be on the order of a GHz, and these are known as Gigahertz Peaked Spectrum (GPS) sources (e.g. Fanti et al. 1995; O’Dea 1998; Randall et al. 2011). The spectral slope can steepen at high frequencies ($\nu_{rest} \gtrsim 10$ GHz) from inverse-Compton losses (e.g. Klammer et al. 2006). Alternatively, a restarting AGN could appear to flatten at high frequencies as the high frequency observations are more sensitive to the flat or inverted AGN core while the lower frequency observations detect the steeper old lobes. Furthermore, thermal (free-free) emission becomes increasingly important at higher frequencies ($\nu_{rest} \gtrsim 10$ GHz) and the relatively flat spectrum of ther-

mal emission can lead to a flattening of the radio SED in starforming galaxies at these frequencies (Condon 1992).

In order to study the spectral curvature of our radio sources we first selected sources which have a $S/N > 10$ in the 5.5 GHz full-band data, to ensure a good detection in each of the four sub-bands. Furthermore we only examined point sources, to limit any effects from the small differences in the beam-sizes of the sub-band images, resulting in a sample of 59 sources. We supplemented the four 6cm sub-bands and VLA 1.4 GHz detections with data from ATLAS 1.4 GHz Data Release 3 (DR3, Franzen et al. 2015 in press). The ATLAS 1.4 GHz DR3 survey covers the full eCDFS at two sub-bands with central frequencies of 1.4 and 1.7 GHz, reaching a typical sensitivity level of $\sim 20 \mu\text{Jy}$ rms with a beam of $16'' \times 7''$ (Franzen et al. 2015 in press). To better explore radio spectral curvature we also include 9 GHz flux densities measured from a 9 GHz image made with CABB 3cm data taken simultaneously with the 6cm data of H12. The 9 GHz image reaches $25 - 30 \mu\text{Jy}$ rms with a beam of $2.9'' \times 1.2''$ (Huynh et al. in prep). The 9 GHz resolution is similar to the VLA 1.4 GHz resolution, however the large beam-size of the ATLAS 1.4 GHz DR3 data could mean discrepant flux densities for sources that are resolved out by the higher resolution images. This should not be a major issue as we are examining only point sources at 5.5 GHz. Furthermore, there is excellent agreement between the VLA 1.4 GHz flux densities and that of ATLAS 1.4 GHz DR3 for $S_{1.4\text{GHz}} > 0.15 \text{ mJy}$ (Franzen et al. 2015 in press).

We fitted the spectral energy distributions in log space with first and second order polynomials of the form:

$$\log S = \gamma + \alpha \log \nu + \beta (\log \nu)^2,$$

with units of S in mJy and ν in GHz. The first order polynomial fit ($\beta = 0$) is the commonly assumed power law $S \propto \nu^\alpha$, with α as the spectral index. We refer to the first order polynomial fit as the log-linear fit and the second order polynomial fit as the log-quadratic fit.

The fitting results for the 59 sources is summarised in Table 5, and their radio SEDs shown in Figure 12. First we compared the spectral index from the log-linear fit to the two point spectral index derived in Section 5.1. We find that the ratio of the two point spectral index to the spectral index from the power law fit to all data, $\alpha_{5.5\text{GHz}-1.4\text{GHz}}/\alpha_{\text{fit}}$, is 1.10 ± 0.04 , with a median of 1.01. Thus the two measures of the spectral index are consistent at the $\sim 10\%$ level. This is reflected in the individual radio SEDs (Figure 12), where the measured full-bandwidth 5.5 GHz flux density (shown as a red diamond) is consistent with the log-linear fit (solid black line).

If the log-quadratic fit is accepted only for $|\beta|/\delta\beta > 2$, i.e. β is formally greater than zero at better than 2σ (95%) level of confidence, then 13/59 (22%) of the 5.5 GHz sources are candidates for sources with significant curvature. These are source IDs 5, 8, 18, 27, 29, 50, 94, 104, 108, 112, 113, 139, 158. On examination of these radio sources 8, 94, 108 and 139 are cases where the 9 GHz detection is low S/N and the SED is consistent with a log-linear fit if the 9 GHz datapoint is discarded, so we conservatively exclude these candidates. Sources 104, 112, and 113 have variable flux densities on timescales of months to years (Bell et al. 2015), so these are excluded also. Source 158 appears to have a positive curvature and the upturn might be due to the 9 GHz obser-

vations picking up the flatter spectrum core of the source. Sources 18, 27, and 50 show negative curvature or steepening spectra. Sources 5 and 29 appear to be GPS sources peaking between 1 to 2 GHz. In summary, the log-quadratic fit is accepted for 6/59 ($\sim 10\%$) of the 5.5 GHz sources after examination, with 1 source showing an upturn, 3 sources showing a steepening, and 2 sources exhibiting a GPS SED peaking between 1 to 2 GHz.

One caveat on these results is that the radio data across 1.4 to 9 GHz were not taken simultaneously and hence source variability can affect the radio SED. Bell et al. (2015) have shown that only a few percent of 5.5 GHz sources are variable on the yearly timescale, and these appear to be inverted spectrum sources where variability is intrinsic to the AGN due to changes in the accretion rate, heating of material and reprocessing of energy by the accretion disk. Hence source variability could explain the SEDs of the GPS candidates, IDs 5 and 29, but it is not a likely explanation for the curvature seen in source IDs 18, 27, 50, and 158.

The fraction of radio sources with significant spectral curvature ranges from almost 100% in the brightest samples (e.g. Laing & Peacock 1980) to 13 – 49% for 1 – 10 mJy level sources (Randall et al. 2012; Ker 2012). This is higher than the fraction we observe in our faint 5.5 GHz sample. We also find 2/59 (3%) sources have a GPS SED, which is lower than the 10% fraction found in Jy level radio samples (O’Dea 1998). This would imply our low flux density sample exhibits less radio spectral curvature than brighter samples, but there are other effects to consider, such as the signal-to-noise ratio of detections, different frequency coverage (greater frequency coverage makes it easier to detect spectral curvature) and the non-consistent definitions of curvature across the different studies. A homogeneous analysis across a large sample of radio sources is required to draw firm conclusions.

6 CONCLUDING REMARKS

We have presented new observations at 5.5 GHz of the extended Chandra Deep Field South with the Australia Telescope Compact Array. Combined with our earlier data, this resulting image of 0.34 deg^2 reaches a noise level of $\sim 8.6 \mu\text{Jy}$ rms, for a synthesized beam of $5.0 \times 2.0 \text{ arcsec}$. This new image is the largest mosaic ever made at this frequency to these depths. Using a false-discovery-rate method, we extracted 189 individual radio sources. Twelve sources were resolved multiple sources with AGN core-lobe or lobe-lobe structures and hence fitted as multiple components.

We derived source counts at 5.5 GHz after careful corrections for completeness, flux boosting and resolution bias. These are amongst the deepest source counts ever calculated at 6cm but come from an area 4 to 7 times larger than the previous surveys to these depths. The ATLAS 5.5 GHz counts are consistent with the counts derived from other 5 GHz surveys at brighter flux densities, but are lower than counts in the literature by a factor of two for $S_{5.5\text{GHz}} < 0.1 \text{ mJy}$. Most of this discrepancy is attributed to cosmic variance because of the small effective area of the surveys at faint flux densities. This fluctuation in the 5.5 GHz source counts at the faint end is similar to that seen at 1.4 GHz for $S_{1.4\text{GHz}} < 0.1 \text{ mJy}$ (e.g. Norris et al. 2011). In general there

Table 5. Summary of radio spectral energy distribution fitting results.

ID	Log-linear fit				Log-quadratic fit					
	γ	$\delta\gamma$	α	$\delta\alpha$	γ	$\delta\gamma$	α	$\delta\alpha$	β	$\delta\beta$
2	0.01	0.03	-0.73	0.09	0.19	0.14	-2.07	1.02	1.48	1.12
3	0.22	0.03	-0.72	0.07	0.21	0.12	-0.65	0.84	-0.08	0.95
4	-0.06	0.04	-1.06	0.10	0.19	0.14	-2.97	1.05	2.17	1.19
5	0.11	0.03	-0.60	0.05	-0.03	0.07	0.40	0.43	-1.06	0.45
8	-0.60	0.05	0.27	0.08	-0.84	0.11	1.93	0.67	-1.79	0.71
10	-0.58	0.05	-0.11	0.09	-0.63	0.19	0.26	1.49	-0.42	1.67
12	-0.25	0.04	-0.51	0.07	-0.26	0.13	-0.44	0.89	-0.07	0.99
16	-0.85	0.06	-0.13	0.13	-0.74	0.25	-1.03	1.98	1.00	2.20
18	0.75	0.03	-0.89	0.04	0.66	0.04	-0.24	0.25	-0.68	0.26
19	0.16	0.03	-0.42	0.04	0.21	0.05	-0.76	0.27	0.35	0.27
21	0.55	0.02	-0.63	0.04	0.48	0.04	-0.17	0.25	-0.47	0.25
22	-0.33	0.03	0.22	0.05	-0.27	0.06	-0.20	0.38	0.44	0.40
23	-0.13	0.04	-0.75	0.09	-0.19	0.14	-0.35	1.01	-0.44	1.13
24	-0.39	0.04	-0.69	0.09	-0.49	0.11	0.11	0.81	-0.89	0.89
26	-0.36	0.04	-0.88	0.10	-0.30	0.24	-1.34	1.90	0.52	2.15
27	1.45	0.02	-0.62	0.03	1.39	0.04	-0.22	0.18	-0.40	0.17
29	0.23	0.03	-0.80	0.05	0.08	0.06	0.29	0.42	-1.19	0.46
40	-1.47	0.15	0.71	0.21	-1.84	0.31	3.58	2.09	-3.21	2.33
44	-0.83	0.07	0.14	0.11	-0.96	0.12	1.03	0.62	-0.94	0.64
50	0.86	0.03	-0.70	0.04	0.79	0.04	-0.23	0.21	-0.47	0.21
57	-0.43	0.05	-0.70	0.11	-0.47	0.21	-0.33	1.67	-0.42	1.88
61	-0.30	0.05	-0.79	0.11	-0.85	0.29	3.76	2.35	-5.25	2.71
62	-0.09	0.03	-1.14	0.09	-0.10	0.11	-1.06	0.74	-0.08	0.82
71	-1.44	0.11	0.63	0.18	-1.07	0.34	-2.36	2.54	3.30	2.81
82	-0.93	0.06	0.09	0.11	-0.89	0.24	-0.22	1.87	0.36	2.13
83	-0.50	0.05	-0.76	0.13	-0.79	0.29	1.61	2.27	-2.69	2.56
84	-0.51	0.06	-0.75	0.13	-0.25	0.18	-2.75	1.38	2.15	1.47
90	-0.34	0.05	-0.86	0.10	-0.30	0.25	-1.17	2.01	0.35	2.28
92	-0.69	0.06	-0.43	0.12	-0.68	0.13	-0.54	0.89	0.12	0.98
94	-0.26	0.03	-0.23	0.06	-0.41	0.07	0.89	0.47	-1.20	0.50
95	0.54	0.02	-0.38	0.04	0.52	0.04	-0.26	0.21	-0.12	0.21
101	-1.41	0.12	0.46	0.18	-1.48	0.18	0.92	1.00	-0.48	1.04
104	0.53	0.02	0.68	0.03	0.34	0.04	1.86	0.18	-1.17	0.18
107	0.53	0.02	-0.29	0.04	0.58	0.04	-0.56	0.21	0.28	0.21
108	-0.39	0.04	-0.45	0.07	-0.23	0.08	-1.71	0.53	1.33	0.55
109	-0.62	0.06	-0.47	0.10	-0.58	0.14	-0.79	1.02	0.34	1.10
112	-0.62	0.05	0.42	0.07	-0.72	0.07	1.04	0.32	-0.63	0.31
113	0.29	0.02	0.30	0.04	0.11	0.04	1.45	0.20	-1.14	0.19
115	1.02	0.02	0.17	0.04	1.00	0.04	0.26	0.19	-0.09	0.19
118	-0.38	0.04	-0.84	0.09	-0.40	0.12	-0.70	0.82	-0.15	0.89
122	0.25	0.03	0.16	0.04	0.20	0.04	0.47	0.22	-0.31	0.22
123	-0.69	0.06	-0.45	0.12	-0.63	0.16	-0.88	1.16	0.47	1.25
129	-0.18	0.03	0.02	0.05	-0.26	0.05	0.54	0.27	-0.53	0.27
130	0.02	0.03	-0.37	0.05	0.08	0.06	-0.77	0.34	0.42	0.35
132	-0.03	0.03	-1.26	0.08	-0.08	0.11	-0.88	0.80	-0.42	0.88
134	-0.62	0.06	-0.27	0.11	-0.66	0.13	0.01	0.89	-0.30	0.95
139	-0.53	0.04	-0.18	0.07	-0.24	0.08	-2.32	0.45	2.17	0.45
152	-0.12	0.04	-0.72	0.08	-0.07	0.13	-1.03	0.93	0.35	1.04
155	-0.32	0.04	-0.57	0.08	-0.50	0.11	0.73	0.76	-1.41	0.82
158	0.78	0.03	-0.69	0.04	0.86	0.04	-1.18	0.24	0.50	0.24
159	-0.02	0.03	-1.04	0.08	-0.07	0.09	-0.65	0.66	-0.43	0.72
162	-0.07	0.04	-1.10	0.10	0.01	0.14	-1.67	1.03	0.65	1.14
163	-0.93	0.06	0.19	0.10	-0.97	0.18	0.50	1.34	-0.35	1.49
173	-0.55	0.06	-0.59	0.12	-0.29	0.32	-2.66	2.50	2.28	2.76
175	-0.25	0.04	-0.94	0.10	-0.49	0.25	1.02	2.02	-2.23	2.29
181	0.26	0.03	-0.78	0.05	0.36	0.06	-1.47	0.38	0.73	0.40
182	-0.85	0.06	0.17	0.10	-1.06	0.14	1.84	1.01	-1.87	1.12
185	-0.56	0.05	0.46	0.08	-0.71	0.11	1.47	0.65	-1.10	0.70
187	-0.68	0.05	-0.17	0.12	-0.68	0.20	-0.20	1.45	0.03	1.60

is good agreement between the observed counts and that of semi-empirical simulations of Wilman et al. 2008, but there maybe an excess in observed sources in the $\sim 0.5 - 2$ mJy flux density range, which may be related to flat-spectrum sources detected at sub-mJy levels at higher frequencies (> 10 GHz, Whittam et al. 2013; Franzen et al. 2014).

The 1.4 – 5.5 GHz spectral index has also been determined for the 5.5 GHz sample. We find a median spectral index for the ATCA 5.5 GHz sample of $\alpha_{\text{med}} = -0.58$. This is steeper than the median spectral index for sub-mJy samples at 5.5 GHz and steeper than our previous result in Data Release 1 (Huynh et al. 2012b). These new deeper observations may be starting to probe the starforming population. However a significant fraction (39%) of the faintest sources ($0.05 < S_{5.5\text{GHz}} < 0.1$ mJy) show a flat or inverted spectral index ($\alpha > -0.5$).

The radio SEDs of the brighter sources ($S/N > 10$) in our 5.5 GHz sample were studied in detail by combining 4 flux density measurements in this work, spanning 4.5 to 6.5 GHz, with literature data at 1.4 and 9 GHz. We fit the radio SEDs with both a log-linear and log-quadratic function to search for significant curvature over 0.8 dex in frequency. The log-quadratic fit is accepted for 10% of the 5.5 GHz sources, with 1 source showing an upturn, 3 sources showing a steepening, and 2 sources exhibiting a GPS SED peaking between 1 to 2 GHz.

New radio facilities are becoming available such as the upgraded VLA (the Karl G. Jansky VLA) and the Square Kilometre Array pathfinders, ASKAP and MeerKAT. In the next few years deep radio surveys will routinely achieve rms sensitivities of $\sim 1\mu\text{Jy}$ at frequencies near 1.4 GHz (e.g. Condon et al. 2012), providing valuable insight into the star formation and AGN activity in galaxies. Higher frequency radio surveys appear to select flat-spectrum populations not present in 1.4 GHz surveys of similar depth. Hence deep observations, at 5 GHz and above, will remain important for a full understanding the faint radio population.

ACKNOWLEDGEMENTS

The ATCA is part of the Australia Telescope which is funded by the Commonwealth of Australia for operation as a National Facility managed by CSIRO. NS is a recipient of an ARC Future Fellowship.

REFERENCES

Aird J. et al., 2010, MNRAS, 401, 2531
 Baars J. W. M., Genzel R., Pauliny-Toth I. I. K., Witzel A., 1977, A&A, 61, 99
 Bell M. E., Huynh M. T., Hancock P., Murphy T., Gaensler B. M., Burlon D., Trott C., Bannister K., 2015, MNRAS, 450, 4221
 Bertin E., Arnouts S., 1996, A&AS, 117, 393
 Bonzini M., Padovani P., Mainieri V., Kellermann K. I., Miller N., Rosati P., Tozzi P., Vattakunnel S., 2013, MNRAS, 436, 3759
 Briggs D. S., 1995, PhD thesis, New Mexico Institute of Mining and Technology

Cileigi P., Zamorani G., Hasinger G., Lehmann I., Szokoly G., Wilson G., 2003, A&A, 398, 901
 Condon J. J., 1984a, ApJ, 287, 461
 Condon J. J., 1984b, ApJ, 284, 44
 Condon J. J., 1989, ApJ, 338, 13
 Condon J. J., 1992, ARA&A, 30, 575
 Condon J. J. et al., 2012, ApJ, 758, 23
 Condon J. J., Cotton W. D., Greisen E. W., Yin Q. F., Perley R. A., Taylor G. B., Broderick J. J., 1998, AJ, 115, 1693
 Condon J. J., Ledden J. E., 1981, AJ, 86, 643
 Cowie L. L., Songaila A., Hu E. M., Cohen J. G., 1996, AJ, 112, 839
 Donnelly R. H., Partridge R. B., Windhorst R. A., 1987, ApJ, 321, 94
 Fanti C., Fanti R., Dallacasa D., Schilizzi R. T., Spencer R. E., Stanghellini C., 1995, A&A, 302, 317
 Fomalont E. B., Windhorst R. A., Kristian J. A., Kellerman K. I., 1991, AJ, 102, 1258
 Franzen T. M. O. et al., 2014, MNRAS, 439, 1212
 Hales C. A., Murphy T., Curran J. R., Middelberg E., Gaensler B. M., Norris R. P., 2012, MNRAS, 425, 979
 Hancock P. J., Murphy T., Gaensler B. M., Hopkins A., Curran J. R., 2012, MNRAS, 422, 1812
 Hasinger G., Miyaji T., Schmidt M., 2005, A&A, 441, 417
 Heywood I., Jarvis M. J., Condon J. J., 2013, MNRAS, 432, 2625
 Hopkins A. M., Beacom J. F., 2006, ApJ, 651, 142
 Hopkins A. M., Miller C. J., Connolly A. J., Genovese C., Nichol R. C., Wasserman L., 2002, AJ, 123, 1086
 Hopkins A. M., Mobasher B., Cram L., Rowan-Robinson M., 1998, MNRAS, 296, 839
 Huynh M. T., Hopkins A., Norris R., Hancock P., Murphy T., Jurek R., Whiting M., 2012a, PASA, 29, 229
 Huynh M. T., Hopkins A. M., Lenc E., Mao M. Y., Middelberg E., Norris R. P., Randall K. E., 2012b, MNRAS, 426, 2342
 Huynh M. T., Jackson C. A., Norris R. P., Fernandez-Soto A., 2008, AJ, 135, 2470
 Huynh M. T., Jackson C. A., Norris R. P., Prandoni I., 2005, AJ, 130, 1373
 Ibar E., Ivison R. J., Biggs A. D., Lal D. V., Best P. N., Green D. A., 2009, MNRAS, 397, 281
 Jarvis M. J., Rawlings S., 2004, NewAR, 48, 1173
 Juneau S. et al., 2005, ApJL, 619, L135
 Kellermann K. I., Fomalont E. B., Mainieri V., Padovani P., Rosati P., Shaver P., Tozzi P., Miller N., 2008, ApJS, 179, 71
 Ker L. M., 2012, PhD thesis, University of Edinburgh
 Klammer I. J., Ekers R. D., Bryant J. J., Hunstead R. W., Sadler E. M., De Breuck C., 2006, MNRAS, 371, 852
 Laing R. A., Peacock J. A., 1980, MNRAS, 190, 903
 Magorrian J. et al., 1998, AJ, 115, 2285
 Miller C. J. et al., 2001, AJ, 122, 3492
 Miller N. A. et al., 2013, ApJS, 205, 13
 Mobasher B. et al., 2009, ApJ, 690, 1074
 Murphy E. J., 2009, ApJ, 706, 482
 Murphy T. et al., 2013, PASA, 30, 6
 Muxlow T. W. B. et al., 2005, MNRAS, 358, 1159
 Norris R. P. et al., 2011, PASA, 28, 215
 O’Dea C. P., 1998, PASP, 110, 493

- Offringa A. R., de Bruyn A. G., Biehl M., Zaroubi S., Bernardi G., Pandey V. N., 2010, *MNRAS*, 405, 155
- Owen F. N., Condon J. J., Ledden J. E., 1983, *AJ*, 88, 1
- Padovani P., Mainieri V., Tozzi P., Kellermann K. I., Formalont E. B., Miller N., Rosati P., Shaver P., 2009, *ApJ*, 694, 235
- Padovani P., Miller N., Kellermann K. I., Mainieri V., Rosati P., Tozzi P., 2011, *ApJ*, 740, 20
- Peacock J. A., Wall J. V., 1981, *MNRAS*, 194, 331
- Prandoni I., Gregorini L., Parma P., de Ruiter H. R., Vettolani G., Wieringa M. H., Ekers R. D., 2001, *A&A*, 365, 392
- Prandoni I., Parma P., Wieringa M. H., de Ruiter H. R., Gregorini L., Mignano A., Vettolani G., Ekers R. D., 2006, *A&A*, 457, 517
- Randall K. E., Hopkins A. M., Norris R. P., Edwards P. G., 2011, *MNRAS*, 416, 1135
- Randall K. E., Hopkins A. M., Norris R. P., Zinn P.-C., Middelberg E., Mao M. Y., Sharp R. G., 2012, *MNRAS*, 421, 1644
- Rowan-Robinson M., Benn C. R., Lawrence A., McMahon R. G., Broadhurst T. J., 1993, *MNRAS*, 263, 123
- Schinnerer E. et al., 2010, *ApJS*, 188, 384
- Schinnerer E. et al., 2007, *ApJS*, 172, 46
- Seymour N. et al., 2008, *MNRAS*, 386, 1695
- Smolčić V. et al., 2008, *ApJS*, 177, 14
- Whiting M. T., 2012, *MNRAS*, 421, 3242
- Whittam I. H. et al., 2013, *MNRAS*, 429, 2080
- Wilman R. J., Jarvis M. J., Mauch T., Rawlings S., Hickey S., 2010, *MNRAS*, 405, 447
- Wilman R. J. et al., 2008, *MNRAS*, 388, 1335
- Wilson W. E. et al., 2011, *MNRAS*, 416, 832
- Windhorst R., Mathis D., Neuschaefer L., 1990, in *Astronomical Society of the Pacific Conference Series*, Vol. 10, *Evolution of the Universe of Galaxies*, R. G. Kron, ed., pp. 389–403
- Windhorst R. A., Miley G. K., Owen F. N., Kron R. G., Koo D. C., 1985, *ApJ*, 289, 494
- Witzel A., Pauliny-Toth I. I. K., Nauber U., Schmidt J., 1979, *AJ*, 84, 942

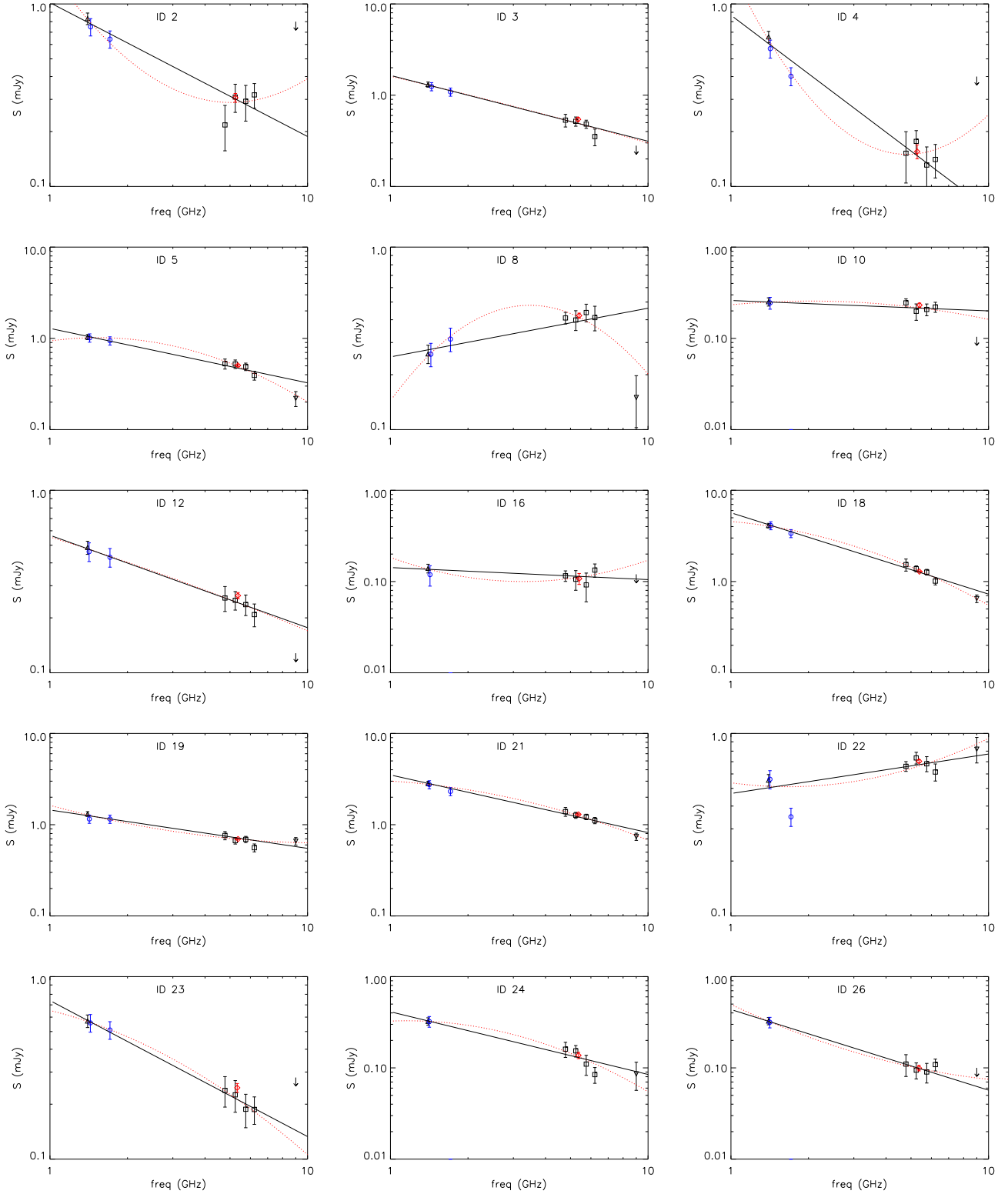


Figure 12. The radio spectral energy distribution for all 6cm sources with S/N greater than 10. The datapoints at 1.4 and 1.7 GHz come from Miller et al. (2013) (black triangles) and Franzen et al. (2015, in press) (blue circles). The four measurements across 4.5 to 6.5 GHz (black squares) are from this work. The 9 GHz datapoint (black upside-down triangle, Huynh et al. 2015 in prep) is shown for sources detected at 9 GHz. An arrow is placed at 4σ in the case of no detection at 9 GHz. The log-linear fit to this data is shown as a solid black line while the log-quadratic fit is shown as the red dotted line. Only $\sim 10\%$ of sources show significant curvature. The red diamond indicates the full-band 5.5 GHz flux densities.

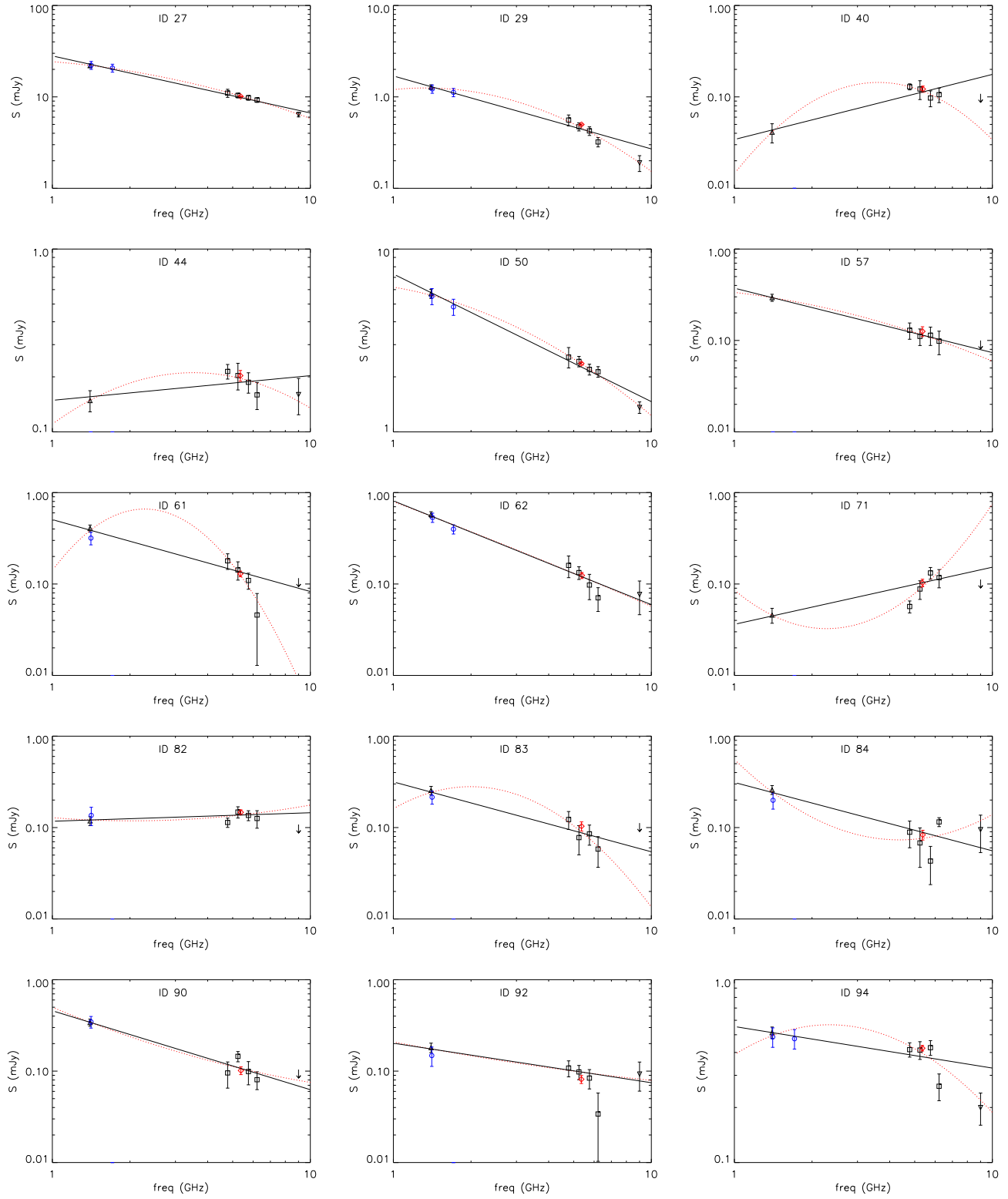


Figure 12 (continued)

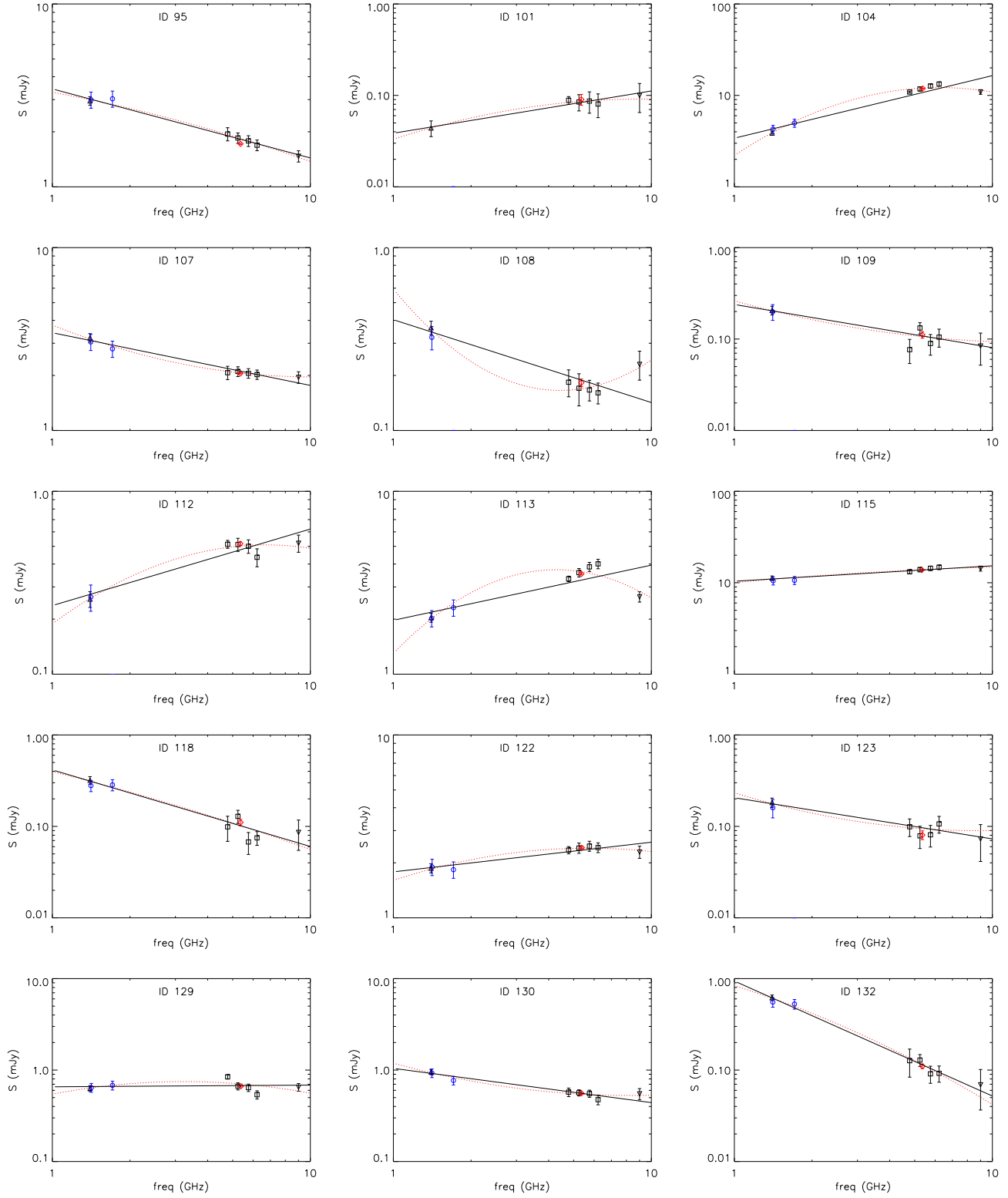


Figure 12 (continued)

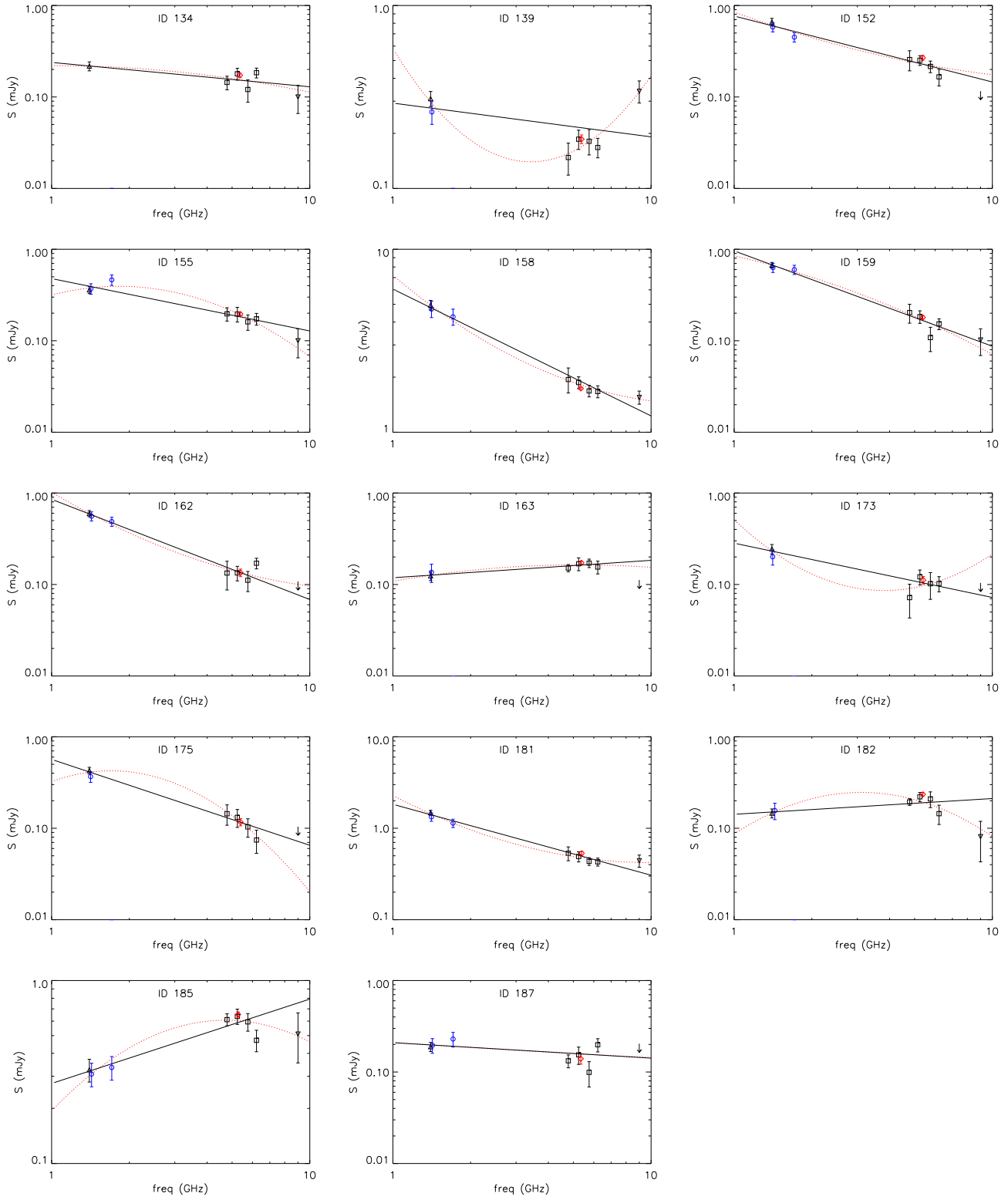


Figure 12 (continued)